Cell

Resource

Whole-organ and whole-body 3D atlases enable cellome-wide profiling

Graphical abstract

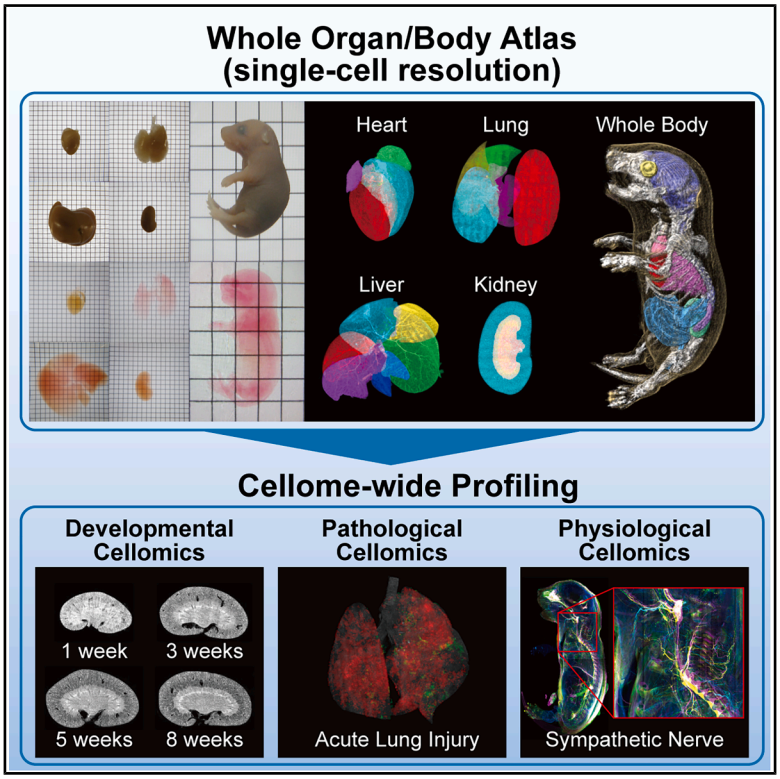

Highlights

- We created organ-/body-wide whole-cell atlases (CUBIC Organ/Body Atlas) of mice
- Each atlas contains all cell coordinates in major organs and a whole neonatal body
- Advanced system rapidly collected single-cell-resolution images across samples
- This resource aids cellomics studies on diseases and developmental processes

Authors

Shota Y. Yoshida, Katsuhiko Matsumoto, Satoshi Takagi, ..., Eiichi Morii, Etsuo A. Susaki, Hiroki R. Ueda

Correspondence

uedah-tky@umin.ac.jp

In brief

Whole-organ and whole-body atlases at single-cell resolution enable quantitative cellome-wide analysis across development, physiology, and pathology.

Yoshida et al., 2026, Cell *189*, 1836–1853
March 19, 2026
https://doi.org/10.1016/j.cell.2025.12.057

CellPress

CellPress

Cell

Resource

Whole-organ and whole-body 3D atlases enable cellome-wide profiling

Shota Y. Yoshida,[1,2,3,4,14] Katsuhiko Matsumoto,[1,2,14] Satoshi Takagi,[5] Fukuaki L. Kinoshita,[1,2,6] Katsunari Yamashita,[1,2,3,7] Daichi Shigeta,[8] Yoshichika Yoshioka,[9] Tetsuo Ushiku,[4] Eiichi Morii,[3] Etsuo A. Susaki,[1,10,11,12] and Hiroki R. Ueda[1,2,7,13,15,*]

[1]Laboratory for Synthetic Biology, RIKEN Center for Biosystems Dynamics Research, Suita, Osaka, Japan
[2]Department of Systems Pharmacology, Graduate School of Medicine, The University of Tokyo, 7-3-1 Hongo, Bunkyo-ku, Tokyo, Japan
[3]Department of Pathology, Osaka University Graduate School of Medicine, Osaka, Japan
[4]Department of Pathology, Graduate School of Medicine, The University of Tokyo, Tokyo, Japan
[5]Division of Experimental Chemotherapy, Cancer Chemotherapy Center, Japanese Foundation for Cancer Research (JFCR), Koto-ku, Tokyo, Japan
[6]Department of Neurology, Graduate School of Medicine, Osaka University, Suita, Japan
[7]Department of Systems Biology, Graduate School of Medicine, Osaka University, 1-3 Yamadaoka, Suita, Japan
[8]Department of Anatomy, Kanazawa Medical University, Uchinada, Ishikawa, Japan
[9]Institute for Biomedical Sciences, Iwate Medical University, Yahaba, Iwate, Japan
[10]Department of Biochemistry and Systems Biomedicine, Graduate School of Medicine, Juntendo University, Tokyo, Japan
[11]Nakatani Biomedical Spatialomics Hub, Graduate School of Medicine, Juntendo University, Tokyo, Japan
[12]Institute for Quantum Life Science, National Institutes for Quantum Science and Technology, Chiba, Japan
[13]Department of Systems Biology, Institute of Life Science, Kurume University, 830-0011, Fukuoka, Japan
[14]These authors contributed equally
[15]Lead contact
*Correspondence: uedah-tky@umin.ac.jp
https://doi.org/10.1016/j.cell.2025.12.057

SUMMARY

Recent advancements in tissue clearing and light-sheet fluorescence microscopy have enabled whole-organ/body-scale analysis at single-cell resolution. However, comprehensive bioinformatics resources like digitized whole-cellome maps, analogous to whole-genome sequencing, remain limited. Here, we present the CUBIC Organ/Body Atlas, a set of three-dimensional single-cell-resolution references for eleven adult mouse organs and a neonatal whole-mouse body. To generate this atlas, we optimized tissue clearing protocols and developed exMOVIE, an imaging system achieving sufficient working distance and axial resolution for organ-/body-wide three-dimensional imaging and subsequent cell nuclei detection. The atlas facilitates comparative analysis among multiple samples at single-cell resolution, allowing for applications in organ development studies, disease state analysis, and whole-body immune cell profiling with three-dimensional immunostaining. Thus, the CUBIC Organ/Body Atlas contributes to establishing a common cellomics workflow, advancing our systems-level understanding of organisms in physiological, developmental, and pathological processes.

INTRODUCTION

Cells are the fundamental units of all living organisms.[1] Understanding the three-dimensional (3D) cytoarchitecture of entire organs and the body improves our knowledge of development, physiology, and disease.[2] Recent 3D pathology studies demonstrate that 2D histology captures only a fraction of structural heterogeneity and often misses rare disease-related cells.[3,4] Even small abnormalities in cellular composition can drive diseases such as cancer,[5] autoimmune disorders,[6] and neurodegenerative diseases.[7] Detecting these rare disease-related cells at the single-cell level is crucial for understanding and addressing the underlying mechanisms of these diseases during their early stages.[8] These challenges require highly sensitive technologies that can analyze entire organs and the whole body at single-cell resolution.

While recent omics advances have expanded our understanding of cellular heterogeneity, each method has limitations. Single-cell sequencing reveals cellular diversity but lacks spatial context because it analyzes dissociated cells.[9] Spatial transcriptomics (ST) has begun addressing this gap,[10] yet most approaches remain 2D and face trade-offs between resolution and molecular coverage. For instance, while Visium HD offers improved resolution, it struggles to detect low-abundance transcripts.[11] Single-molecule fluorescence *in situ* hybridization (FISH)-based methods (e.g., Xenium, CosMx, MERFISH) provide high spatial

resolution but are dependent on accurate cell segmentation.[12] In contrast, imaging-based 3D histology offers an alternative for collecting comprehensive spatial information.[13,14] Cellomics, analyzing the entire set of cell populations in a multicellular system (i.e., cellome), utilizes spatial context to provide a comprehensive view of cellular organization.[14] This approach allows imaging of all cells while preserving their spatial relationships, enabling clustering based on intrinsic spatial information.

Tissue clearing combined with light-sheet fluorescence microscopy (LSFM) has enabled whole-organ and whole-body 3D histology and cellomics.[15–17] Tissue clearing combined with LSFM imaging was first applied to the guinea pig cochlea[18] and later extended to mouse brain.[19] Since then, applications have accumulated across various research fields, including neuroscience,[20,21] developmental biology,[22] cancer,[23] and drug discovery.[24] While dozens of modern tissue clearing protocols have been developed,[25,26] part of them with strong clearing efficiency, such as BABB (benzyl alcohol-benzyl benzoate),[27] 3DISCO (3D imaging of solvent-cleared organs),[28] CUBIC (clear, unobstructed brain imaging cocktails and computational analysis),[29] MACS (MXDA-based aqueous clearing system),[30] CLARITY (clear, lipid-exchanged, anatomically rigid, imaging/immunostaining compatible, tissue hydrogel),[31] and SHIELD (stabilization under harsh conditions via intramolecular epoxide linkages to prevent degradation),[17] can be particularly utilized for whole-organ/-body 3D imaging with LSFM. As such clearing techniques have advanced, LSFM systems for cleared samples have been parallelly developed.[32–36] For example, techniques such as tiling LSFM,[37] axially swept light-sheet microscopy (ASLM),[38] and the moving observation with efficient real-time autofocus (MOVIE) system[39] have contributed to improving the axial resolution, enabling micron- to submicron voxel imaging of entire organs. ExA-SPIM (expansion-assisted selective plane illumination microscopy) has also achieved submicron voxel resolution across a huge, expanded mouse brain.[40]

To perform whole-cellome analysis, a standardized computational pipeline for comparison, clustering, and biological interpretation is essential. A representative example is whole-brain c-Fos mapping, which compares multiple samples after correcting brain size, shape, and orientation.[21,41–46] This method involves mapping detected cell coordinates and intensities onto an atlas, enabling quantification by specific brain regions. However, widely used volumetric atlases, such as the Allen Brain Atlas,[47] lack single-cell resolution and rely on predefined anatomical boundaries. To overcome these limitations, we previously developed the CUBIC Brain Atlas , a coordinate-based single-cell atlas of the mouse brain that uncovered drug-responsive hippocampal subregions and heterogeneous c-Fos activity in the paraventricular thalamus.[42,43] The importance of high-resolution atlases has also been demonstrated by Blain et al., whose 3D cellular atlas uncovered structures not detected by conventional histology.[48] However, such single-cell-resolution atlases for other organs and the whole body had not yet been established.

In this study, we present the CUBIC Organ/Body Atlas, a comprehensive set of single-cell-resolution atlases covering major adult mouse organs and the whole neonatal body. To generate these resources, we developed a specialized LSFM system (exMOVIE [extended MOVIE]) capable of high-speed acquisition with long working distance and improved axial resolution, enabling imaging of hundreds of millions of cells. We also optimized CUBIC clearing for eleven adult organs and the neonatal body, achieving uniformly transparent samples. Using these atlases, we performed whole-organ single-cell profiling to analyze kidney development and drug-induced injury in the kidney and lung. We further mapped IBA1-positive immune cells onto the CUBIC Body Atlas, demonstrating accurate cell-type annotation. Therefore, the CUBIC Organ/Body Atlas expands the capacity for whole-organ and whole-body single-cell analysis and broadens the applications of cellomics across biomedical research.

RESULTS

Optimization of tissue clearing procedures for each whole organ and the whole neonatal body

The original CUBIC Brain Atlas was constructed using ScaleCUBIC-1 for delipidation and CUBIC-X for clearing, where the identification of antipyrine enabled both tissue expansion and a high refractive index (RI).[42] However, because many organs require an RI of approximately 1.50–1.55,[25] the final RI of CUBIC-X (1.467) was insufficient for whole-organ transparency. To address this, we previously developed CUBIC-L, which provides more efficient delipidation, and CUBIC-R+ (RI = 1.52), which achieves an adequate RI while maintaining the expansion properties of CUBIC-X.[49] Consequently, for the creation of CUBIC Organ/Body Atlases in this study, we adopted a clearing protocol using CUBIC-L/R+.

While the original protocol[39] worked for most organs, deeper regions of some tissues lacked sufficient transparency for single-cell-resolution LSFM imaging. Therefore, we optimized the CUBIC-L/R+ clearing workflow for each organ and for whole-body samples (Figures 1A, 1C, and S1A). In the kidney, extended delipidation markedly improved clarity, whereas in the liver, we refined the CUBIC-R+ replacement steps by increasing concentration in 20% increments rather than the standard 50%. For whole neonatal bodies, we incorporated decalcification and hydrogen peroxide bleaching to clear bones and pigmented eyes, adjusting peroxide concentration to minimize bubble formation (Figure S1B). Despite these additional steps, CUBIC-based 3D immunostaining[50] remained compatible with representative antibodies (Figures S1C–S1F; Video S1). Consequently, we achieved sufficient clearing of adult mouse thyroid, salivary glands, heart, lungs, liver, pancreas, kidneys, bladder, epididymis, testis, and uterus, as well as the whole neonatal mouse body (Figures 1B and 1D).

Development of exMOVIE system for whole-organ single-cell-resolution imaging

A major challenge in whole-organ and whole-body imaging was the absence of a microscope capable of rapidly acquiring cellular-resolution images from samples thicker than 20 mm. Such imaging requires an objective lens that combines high magnification with a long working distance suitable for thick organs like the liver, sufficient axial resolution to detect nuclei, and high-speed acquisition to manage terabyte-scale datasets.

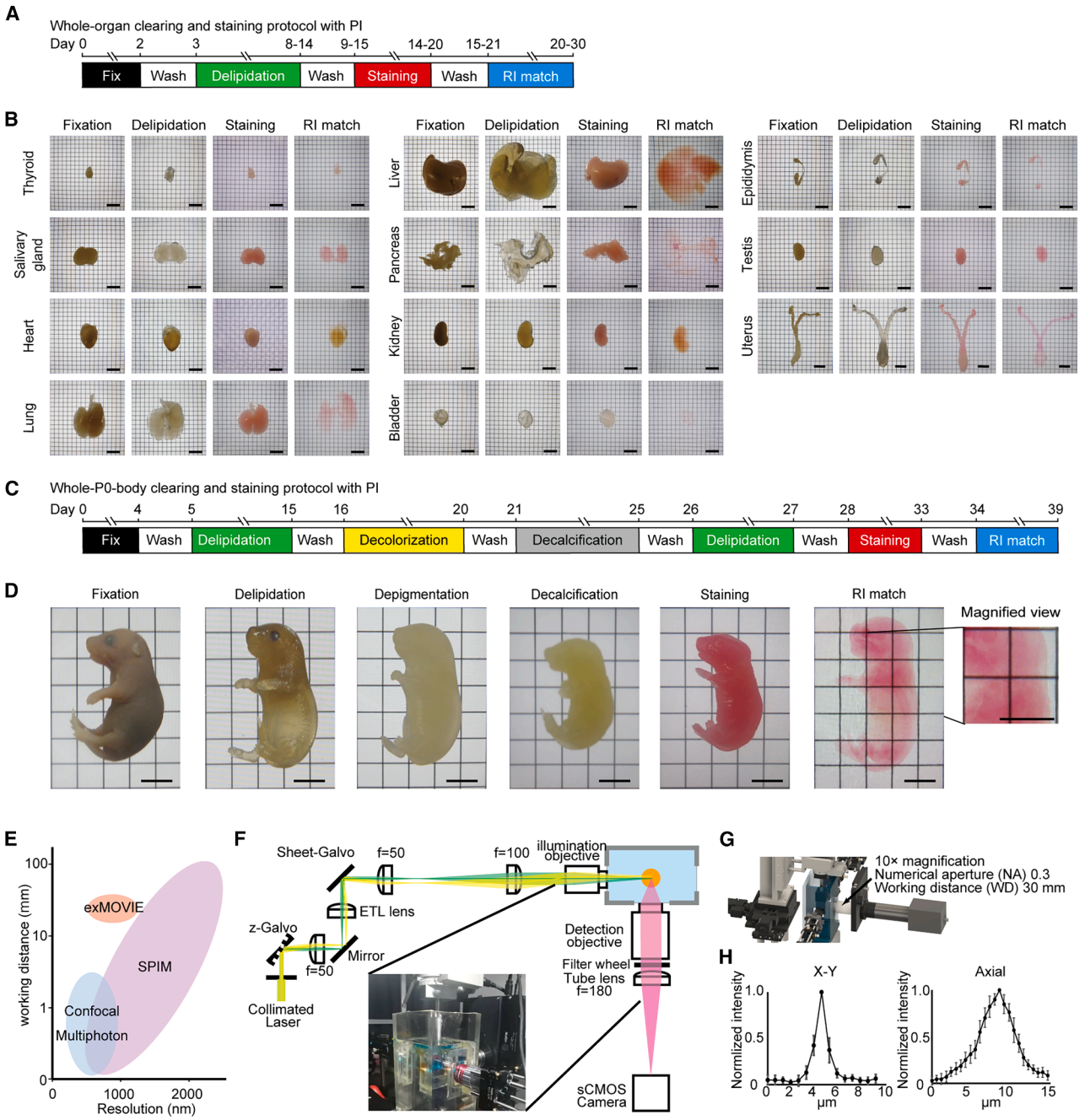

Figure 1. Tissue clearing of ten mouse organs and whole neonatal mice with CUBIC and 3D imaging with exMOVIE system

(A) Timeline of the whole-organ clearing and staining protocol (see also Figure S1A).

(B) Bright-field images of whole organs from an 8-week-old C57BL/6N mouse at each step of the protocol. Scale bars, 5 mm.

(C) Timeline of the whole-body clearing and staining protocol for P0 mice.

(D) Bright-field images of the whole body of a C57BL/6N mouse (P0, male) at each step of the protocol. Scale bars, 5 mm.

(E) Comparison of 3D imaging systems illustrating the trade-off between working distance and resolution.

(F) Schematic of the exMOVIE system, showing the integration of axial light-sheet microscopy and real-time autofocus for high-speed, high-resolution imaging of large organ samples.

(G) CAD model of the exMOVIE system configuration.

(H) Normalized intensity plots showing the full width at half maximum (FWHM) resolution achieved by the exMOVIE system (approximately 1 μm x-y and 5 μm axial). Error bars represent mean ± standard deviation (SD).

See also Figure S1.

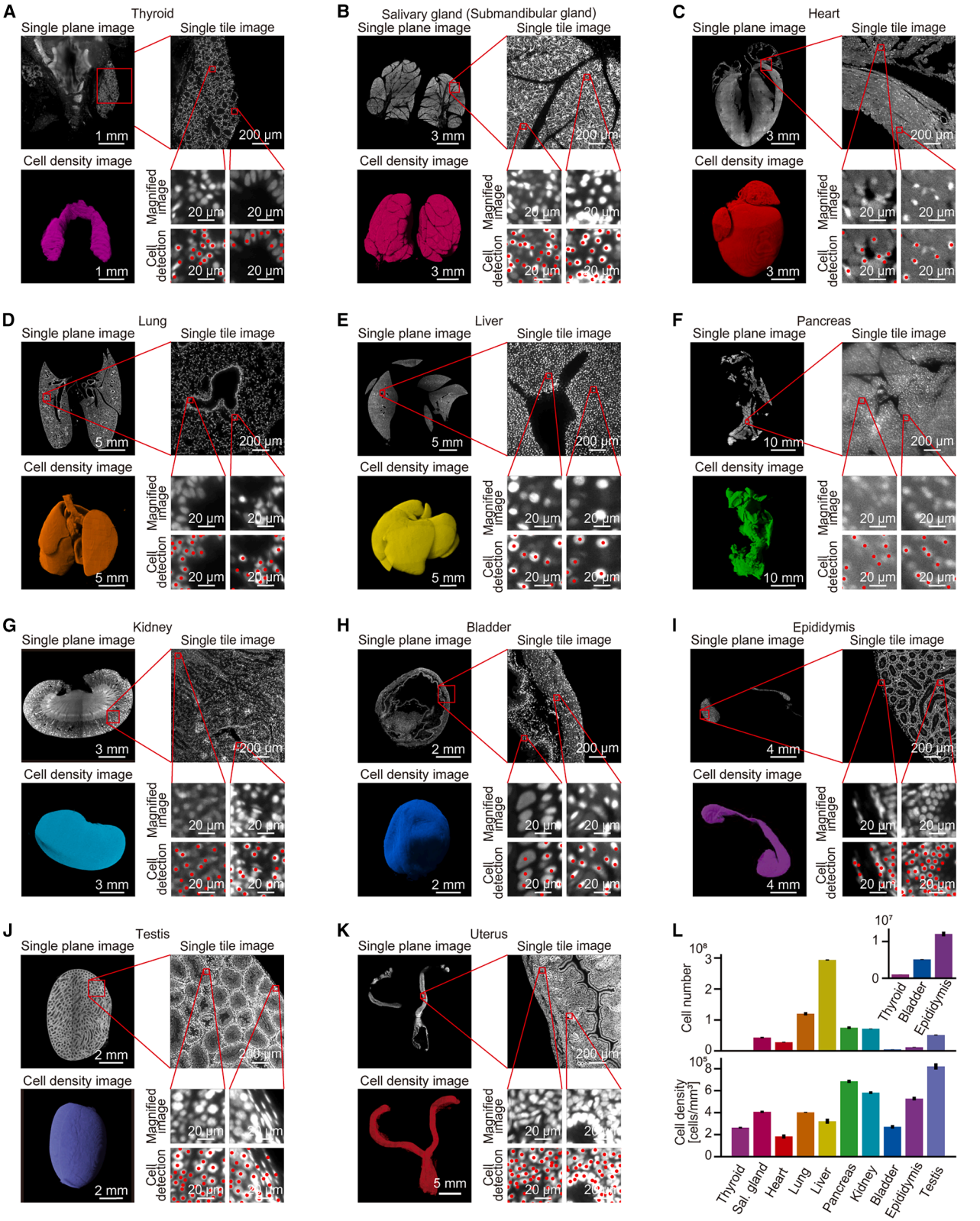

(legend on next page)

Together, these requirements created a substantial technical barrier to cellular-resolution imaging of intact organs and bodies (Figure 1E).

To overcome these obstacles, we developed a light-sheet fluorescence microscope, named exMOVIE, which achieves long working distance, high resolution, and rapid imaging for single-cell-level acquisition of large organs and whole bodies (Figure 1F). The system uses an objective lens with 10× magnification, NA (numerical aperture) 0.3, and a 30-mm WD (working distance) (Figure 1G). High-speed imaging is enabled by combining an sCMOS camera capable of 50 frames per second with the MOVIE autofocus system. In addition, axial resolution was improved by incorporating elements of ASLM[38]. This integration enabled 3D imaging speeds of up to 33 fps with real-time autofocusing while maintaining approximately 1 μm x-y and 5 μm axial full width at half maximum (FWHM) resolution across the entire field of view (Figure 1H).

The exMOVIE system enabled whole-organ and whole-body imaging at 0.65 × 0.65 × 2.5 μm voxel resolution. For example, the liver, which generates the largest dataset among all organs, required approximately 14 TB at 16-bit depth, and exMOVIE acquired the entire dataset in approximately 48 h. These advances in coverage, imaging speed, and resolution made comprehensive single-cell-resolution imaging of whole organs feasible within a practical time frame.

Construction of the CUBIC Organ Atlas

Using the optimized clearing protocols and the exMOVIE system, we acquired single-cell-resolution 3D images of eleven adult mouse organs—thyroid, salivary gland, heart, lung, liver, pancreas, kidney, bladder, epididymis, testis, and uterus—during proestrus. Cell coordinates were extracted from nuclear-stained images using GPUs, achieving high detection accuracy across organs (true positive rate [TPR]: 88%–100%; positive predictive value [PPV]: 87%–100%; Figures S2A–S2J). Accuracy in dense tissues also remained high, with F1 scores above 90% (Figures S2K–S2P).

Because high-magnification LSFM provides a limited field of view, each organ was imaged as overlapping x-y tiles from both sides. To process these large datasets and correct geometric distortions (e.g., stage misalignment, pitching, yawing), we developed a stitching and registration workflow optimized for large-volume 3D data (Figure S3). Existing software such as BigStitcher[51] and TeraStitcher[52] did not support the 3D point cloud alignment required by our pipeline. Our workflow enabled accurate reconstruction of complete 3D point clouds for every organ (Figures 2A–2K).

The resulting CUBIC Organ Atlas provides a full 3D spatial reference of all cells in each organ. Cell numbers ranged from $1.02 \times 10^6 \pm 1.42 \times 10^4$ (thyroid) to $2.94 \times 10^8 \pm 1.64 \times 10^6$ (liver) (Figure 2L). Because CUBIC clearing induces tissue deformation, organ-specific MRI-based volume normalization was applied (Figures S4A–S4H). Normalized cell densities ranged from $1.83 \times 10^5 \pm 1.79 \times 10^4$ cells/mm^3 (heart) to $8.21 \times 10^5 \pm 2.75 \times 10^4$ cells/mm^3 (testis) (Figures 2L and S4I). These densities reflected characteristic cytoarchitecture; the lung and liver showed lower values due to alveolar space and sinusoidal networks,[53,54] while the testis exhibited the highest density, consistent with the tight organization of Sertoli and germ cells during spermatogenesis.[55]

Parenchymal organs with well-defined structures are suited for registration and comparative analysis. To demonstrate this, we generated anatomical segmentations for the heart, lung, liver, and kidney within the CUBIC Organ Atlas (Figure 3A). Whereas construction of the CUBIC Brain Atlas was based on 3D segmented data from the Allen Brain Atlas,[42] no equivalent segmentation existed for these organs, requiring us to generate such datasets *de novo*. We constructed them by defining region boundaries from 3D cell density distributions and reconstructing them as segmented volumes.[56,57] Each detected nucleus was then annotated according to these regions, enabling organ-wide spatial analysis. Using this approach, the heart was divided into the four chambers,[58] the lung into five lobes,[59] the liver into six lobes,[60] and the kidney into three regions.[61] Segmented atlases for female organs were also created using the same workflow (Figures 3B, 3C, and S5).

We next demonstrated multi-sample comparison using the region-annotated CUBIC Organ Atlas (Figure 3D). Hearts, lungs, livers, and kidneys were additionally collected from two adult male C57BL/6N mice (8 weeks old), and cell density images were generated from their 3D point clouds. Samples were mapped to the atlas by first registering whole-organ density images and then applying the resulting matrix to the point clouds, aligning the sample coordinates with the CUBIC Organ Atlas. Each sample cell was subsequently assigned to the nearest atlas cell, thereby inheriting the annotated regional information.

For the heart and kidney, whole-organ registration using affine and symmetric diffeomorphic image registration (SyN) algorithms in ANTs (advanced normalization tools) provided accurate spatial mapping. In contrast, the lungs and livers showed substantial shape variability that hindered whole-organ registration. To address this, we adopted a lobe-by-lobe strategy, dividing each organ's 3D point cloud into individual lobes for registration (Figures S6A and S6B). To increase robustness, we generated average organ templates by averaging images from multiple animals. For each organ, templates were created from male ($n = 3$) and female ($n = 3$) samples; however, the liver exhibited substantial sex-specific differences in shape, necessitating separate male and female templates. All templates are publicly available

Figure 2. Whole-organ single-cell imaging and cell detection in 10 mouse organs

(A–K) Comprehensive cellular detection in organs from C57BL/6N mice (8 weeks old), including thyroid (A), salivary gland (B), heart (C), lung (D), liver (E), pancreas (F), kidney (G), bladder (H), epididymis (I), testis (J), and uterus during proestrus (K). Each panel shows a 2D single-plane image (top left), an enlarged tile from the 2D image (top right), magnified views with detected cells highlighted in red (bottom right), and a 3D cell density image (bottom left).

(L) Cell numbers (top) and cell densities (bottom) for each organ from 8-week-old mice. Densities of all organs, except the thyroid, were corrected using MRI data (see also Figure S4). Error bars represent mean ± SD.

See also Figures S2–S4.

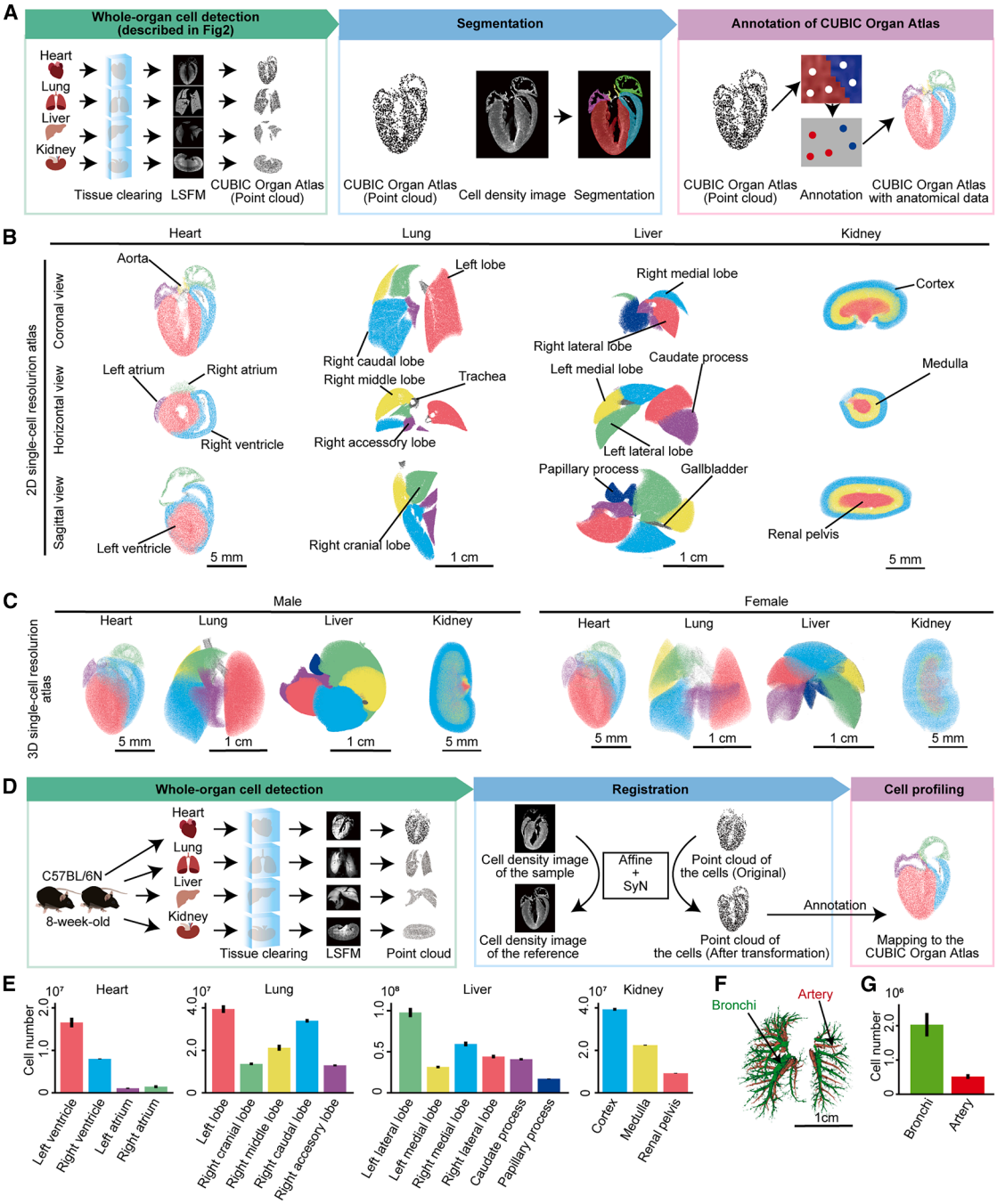

Figure 3. Construction of annotated CUBIC Organ Atlas for comparative analysis

(A) Workflow for generating the region-annotated CUBIC Organ Atlas.

(B) 2D segmented views of anatomical regions in the heart, lung, liver, and kidney.

(C) 3D renderings of segmented anatomical regions in the heart, lung, liver, and kidney from male (left) and female (right) mice.

(D) Workflow for profiling of all cells in the heart, lung, liver, and kidney of 8-week-old male C57BL/6N mice, using the CUBIC Organ Atlas.

(E) Quantification of cell numbers across anatomical regions in the heart, lung, liver, and kidney. Error bars represent mean ± SD.

(F) 3D segmentation of bronchi and arteries in the lung.

(G) Quantification of cell numbers in bronchi and arteries. Error bars represent mean ± SD.

See also Figures S5 and S6.

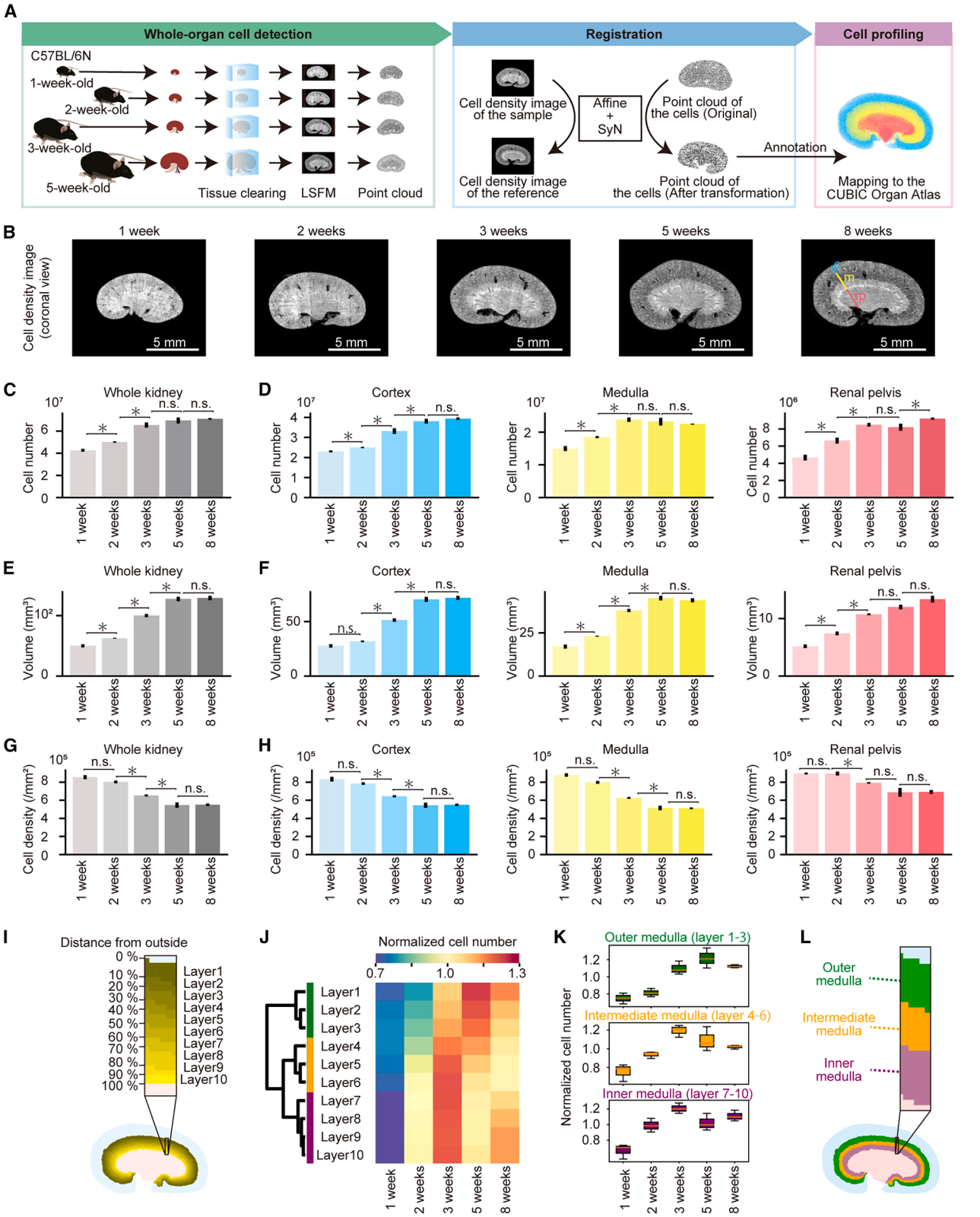

(legend on next page)

(https://whole.cfosdb.systems-based-medicine.org/whole_body/) to support broader application of registration workflows.

We then profiled cell numbers across anatomical regions (n = 3, including atlas datasets) (Figure 3E). These analyses clarified multicellular organization and structure-function relationships within each organ. For example, the left ventricle contained a greater number of cells than other cardiac regions, likely reflecting its higher mechanical workload.[62] In the lung, bronchi and arteries were segmented using 3D Slicer software, and cell numbers were quantified for each region (Figures 3F and 3G). Segmentation accuracy was validated by α-smooth muscle actin (α-SMA) immunostaining, which labels smooth muscle in both structures. The comparison yielded an F1 score of approximately 90%, confirming that nuclear-based segmentation was sufficiently accurate in these tissues (Figures S6C–S6E). Bronchi contained substantially more cells than arteries, consistent with the dense epithelium lining the bronchial wall.[63] These results demonstrate that the CUBIC Organ Atlas can serve as a standardized reference for cellome-wide comparisons across samples, similar to its use in whole-brain analyses.[42,43]

To assess atlas generalizability, we tested registration using organs cleared with BABB, a solvent-based method that induces tissue shrinkage (Figure S6F). The lung and kidney were successfully aligned to the CUBIC Organ Atlas. In the heart, however, severe deformation of the left atrium prevented accurate registration in that region. These findings indicate that the atlas is compatible with alternative clearing protocols, although registration accuracy may decline when distortion is severe.

The CUBIC Organ Atlas enables whole-organ single-cell profiling of mouse kidneys at various developmental stages

To demonstrate the use of the CUBIC Organ Atlas in developmental biology, we quantified changes in cell numbers during kidney development using kidneys from C57BL/6N male mice at 1, 2, 3, 5, and 8 weeks of age (n = 3 per time point) (Figure 4A). Kidneys from 1- to 5-week-old mice were registered to the 8-week Atlas template, and both 3D cell density images and point clouds were aligned to obtain regional information for each cell. Clear differentiation of the cortex, medulla, and renal pelvis became apparent after 3 weeks (Figure 4B). Cell number changes differed by region (Figures 4C and 4D); total kidney cell numbers, as well as those in the cortex and pelvis, increased steadily, whereas medullary cell numbers plateaued by 3 weeks.

We next calculated the volume of the whole kidney and its regions (Figures 4E and 4F). Kidney volume increased continuously until 5 weeks, with early growth (1–2 weeks) driven largely by the medulla and pelvis and later changes (3–5 weeks) mainly reflecting expansion of the cortex and medulla. Cell density decreased with age and stabilized by 5 weeks (Figures 4G and 4H). Given concurrent increases in both cell numbers and volumes, this density reduction suggests additional contributors to volume growth, such as cell and tissue maturation. The medulla showed a particularly distinct pattern; although its cell number no longer increased between 3 and 5 weeks, its volume continued to expand, leading to reduced density. This is consistent with the known developmental timeline in which medullary structures are established by 3–4 weeks in mice,[64,65] implying substantial maturation during this period.

To analyze medullary development in more detail, we divided the medulla into 10 layers based on the outer-inner axis and performed hierarchical clustering with Ward's method (Figures 4I and 4J). Three clusters emerged: one peaking at 5 weeks, another at 3 weeks, and a third showing a bimodal pattern with peaks at 3 and 8 weeks (Figures 4K and 4L). These results show that the CUBIC Organ Atlas enables both region-specific and region-independent analyses of cell number dynamics during development.

The CUBIC Organ Atlas enables whole-organ single-cell profiling in pathological studies

To demonstrate the utility of the CUBIC Organ Atlas in pathology, we performed whole-organ single-cell analysis of drug-induced injury in the kidney and lung (Figure 5A). To model kidney injury, we administered cisplatin intraperitoneally—an anticancer drug with known nephrotoxic effects.[66] Mice were divided into a cisplatin-treated group (n = 3) and a control group (n = 3) that received intraperitoneal saline (Figure 5B). Then, 72 h after the administration, the kidneys were collected, and their nucleus point cloud data were registered to the CUBIC Organ Atlas. As expected from cisplatin's toxicity to proximal renal tubules in the cortex,[67] both total and regional cell numbers were significantly reduced in cisplatin-treated mice, with the largest decrease in the cortex (Figures 5C and 5D). In contrast, glomerular numbers did not significantly differ (Figure 5E), indicating predominant injury to tubular structures. To assess damage independent of predefined anatomical regions, we quantified local cell numbers using a 50 μm × 50 μm × 50-μm kernel. This analysis revealed widespread decreases in the renal cortex (Figure 5F).

Lipopolysaccharide (LPS), a component of Gram-negative bacteria, activates inflammatory pathways and induces immune cell accumulation in the lung.[68] However, whether these

Figure 4. The CUBIC Organ Atlas enables whole-organ single-cell profiling of mouse kidneys at various developmental stages

(A) Workflow for cell profiling in kidneys from C57BL/6N male mice at 1, 2, 3, and 5 weeks of age.

(B) Coronal views of cell density images at each developmental stage (c, cortex; m, medulla; rp, renal pelvis).

(C–H) Quantification of total cell numbers, volume, and cell density for whole kidneys (C, E, and G) and for anatomical regions (cortex, medulla, renal pelvis; D, F, and H). Kidney volumes were corrected using *in vivo* MRI data to account for expansion during tissue clearing (see also Figure S4). *$p < 0.05$; n.s., not significant; statistical tests: negative binomial distribution for cell numbers and Student's t test for volume and cell density (n = 3 per stage).

(I–L) Detailed analysis of medulla development (n = 3 per stage). The medulla was divided into 10 layers based on distance from the outer to inner medulla (I). Hierarchical clustering identified three major clusters (J), corresponding to distinct developmental patterns in the outer, intermediate, and inner layers. Normalized cell numbers in these regions showed characteristic temporal changes (K and L).

Error bars represent mean ± SD.

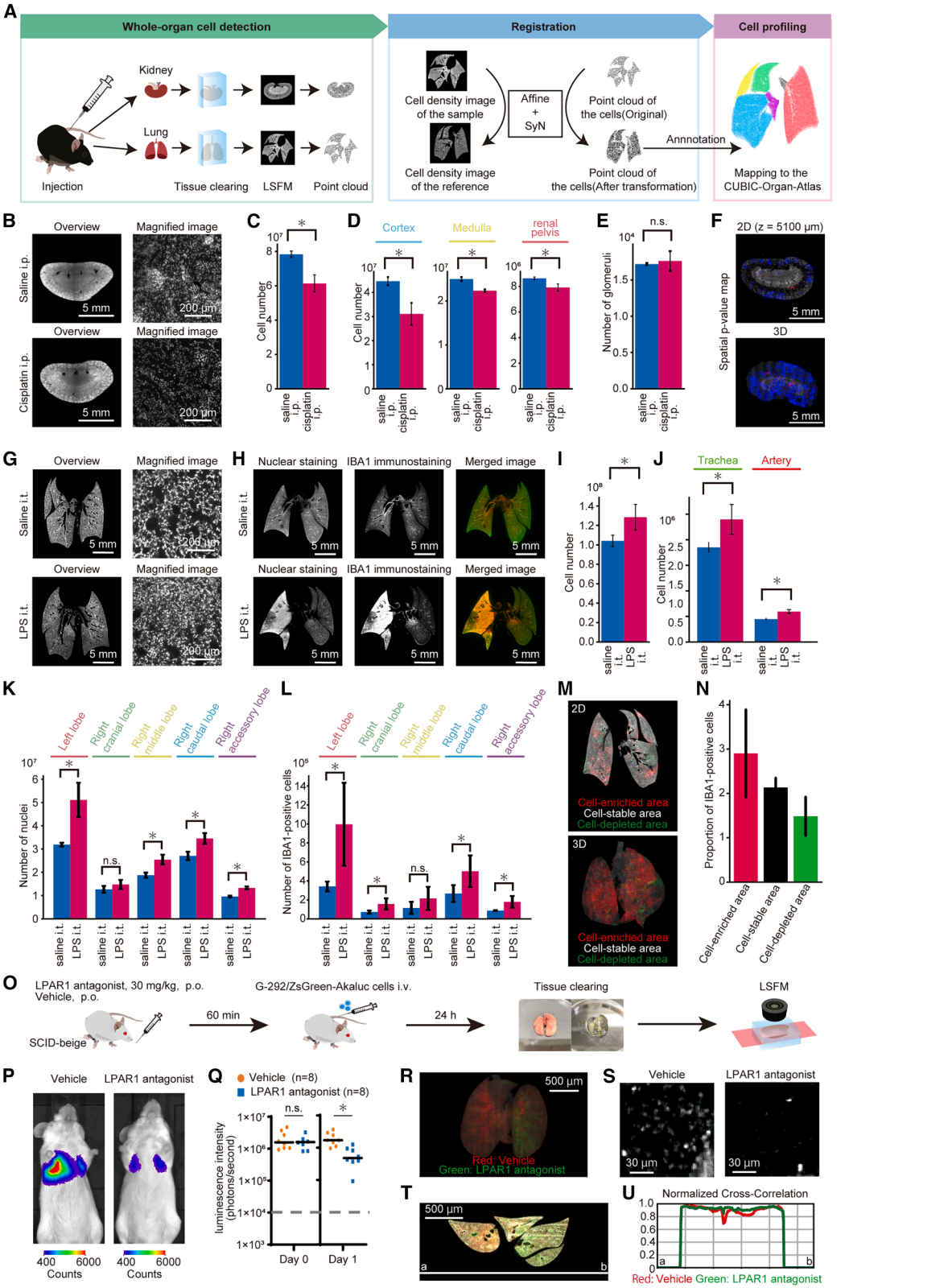

(legend on next page)

responses occur diffusely or in spatially restricted regions has remained unclear. To address this question, we applied our cellomics workflow using the CUBIC Organ Atlas. LPS was administered intratracheally to induce acute lung injury (ALI) ($n = 3$), and saline was administered to control mice ($n = 3$). Afterward, 96 h after administration, nuclear-stained images revealed localized increases in cellularity (Figure 5G). To further characterize the inflammatory response, we simultaneously stained nuclei and IBA1, a marker of macrophages; dendritic cells; and monocytes (saline, $n = 3$; LPS, $n = 4$) (Figure 5H). Quantitative analysis confirmed a significant increase in total lung cell numbers after LPS administration (Figure 5I). Cell numbers in regions adjacent to the trachea and arteries also showed marked increases (Figure 5J). Cell number changes varied across anatomical lobes; the right cranial lobe showed no significant change, whereas other lobes exhibited substantial increases (Figure 5K). Analysis of IBA1-positive cells revealed significant increases in all lobes except the right middle lobe (Figure 5L). To evaluate the spatial relationship between cellularity and immune cell recruitment, lung tissue was classified into cell-enriched, cell-stable, and cell-depleted areas (Figure 5M). We found that cell-enriched area exhibited the highest proportion of IBA1-positive cells (Figure 5N). These results indicate that the LPS-induced increase in cell number is partly attributable to the accumulation of IBA1-positive immune cells.

We also tested the applicability of the CUBIC Organ Atlas in more general experimental situations, in which the samples observed, using lower-magnification LSFM (0.63×/NA 0.15), and the fluorescence intensities were compared instead of cell counts. Mice were orally administered an LPAR1 (lysophosphatidic acid receptor 1) antagonist (ONO-7300243) or vehicle, followed by intravenous injection of G-292/ZsGreen-Akaluc-expressing G-292 osteosarcoma cells to model lung metastasis (Figure 5O). LPAR1 is required for platelet-dependent enhancement of osteosarcoma invasiveness, and its inhibition suppresses pulmonary metastasis.[69] Indeed, the *in vivo* luminescent signals 24 h after the administration showed that the cells were mainly distributed in the lung, and the LPAR1 antagonist significantly reduced the signals (Figures 5P and 5Q). To compare their signal distributions, we then mapped them to the CUBIC Organ Atlas to merge their signals. The resulting image revealed a cluster of tumor cells in the left lobe of the lung in the group without LPAR1 antagonist treatment, which was reduced in the group treated with the LPAR1 antagonist (Figure 5R). Higher-magnification views confirmed more aggregated tumor cells in the vehicle group (Figure 5S). Despite different genetic backgrounds between tumor-bearing mice and the C57BL/6N reference, registration succeeded, demonstrating that the atlas is robust to moderate genetic variation and is broadly applicable to user-driven studies (Figures 5T and 5U).

Construction of the CUBIC Body Atlas

To construct the CUBIC Body Atlas, we imaged cleared and nuclear-stained neonatal C57BL/6N mice. The high-speed imaging capability of exMOVIE enabled acquisition of 20 TB of whole-body data within 72 h, yielding sufficient images for cell counting throughout the body (Figures 6A and 6B). Cell detection and stitching followed the same workflow used for the CUBIC Organ Atlas (Figure S5). Detection performance achieved a TPR of 89%–100% and a PPV of 84%–100% across neonatal organs. In total, $6.14 \times 10^8 \pm 2.76 \times 10^6$ cells were detected in male post-natal day 0 (P0) mice ($n = 3$), whereas $5.31 \times 10^8 \pm 1.42 \times 10^7$ cells were detected in female P0 mice ($n = 3$). One male dataset was selected as the reference CUBIC Body Atlas.

To segment organs, we generated a 3D nuclear density image as in the CUBIC Organ Atlas. The bones, skin, eyes, thymus, lung, heart, liver, spleen, brain, spinal cord, intestine, kidneys, and bladder were segmented, and each detected nucleus was assigned to the corresponding region (Figures 6C and 6D; Video S2). Representative regions were examined to

Figure 5. The CUBIC Organ Atlas enables whole-organ single-cell profiling in pathological studies

(A) Workflow for cell profiling in the kidney and lung following drug-induced damage.

(B) Representative 2D kidney images from saline- and cisplatin-treated mice with magnified views.

(C–E) Comparisons of total cell numbers (C), regional cell numbers (D), and glomerular counts (E) between saline- and cisplatin-treated groups. $^*p < 0.05$; n.s., not significant; statistical test: negative binomial distribution ($n = 3$).

(F) 2D (top) and 3D (bottom) voxel-wise p value maps showing regions with significantly decreased (blue) or increased (red) cell numbers in cisplatin-treated kidneys.

(G) Representative 2D lung images from saline- (top) and LPS-treated (bottom) mice with magnified views.

(H) Representative lung images showing nuclear staining (left), IBA1 immunostaining (middle), and merged signals (right) in saline- (top) and LPS-treated (bottom) groups.

(I and J) Quantification of total lung cell numbers (I) and cell numbers in trachea- and artery-adjacent regions (J). $^*p < 0.05$; n.s., not significant; statistical test: negative binomial distribution ($n = 3$).

(K and L) Quantification of total cell numbers (K) and IBA1-positive cell numbers (L) in each lung lobe for saline- and LPS-treated mice. $^*p < 0.05$; n.s., not significant; statistical test: negative binomial distribution (saline, $n = 3$; LPS, $n = 4$).

(M) 2D (top) and 3D (bottom) visualization of lung tissue categorized into cell-enriched (red), cell-stable (gray), and cell-depleted (green) regions.

(N) Proportion of IBA1-positive cells within cell-enriched, cell-stable, and cell-depleted regions.

(O) Workflow of the imaging of the lung metastasis model.

(P) *In vivo* luminescence imaging showing reduced tumor burden in LPAR1 antagonist-treated mice relative to vehicle controls.

(Q) Quantification of luminescence intensity at days 0 and 1. $^*p < 0.05$; n.s., not significant; statistical test: Mann-Whitney U test ($n = 8$).

(R) 3D visualization of lung images registered to the CUBIC Organ Atlas.

(S) Higher-magnification LSFM images showing denser tumor cell clusters in vehicle-treated lungs compared with LPAR1 antagonist-treated lungs.

(T) Registration of vehicle-treated (red) and LPAR1 antagonist-treated (green) lung images to the CUBIC Organ Atlas.

(U) Quantitative assessment of registration accuracy using normalized cross-correlation.

Error bars represent mean ± SD.

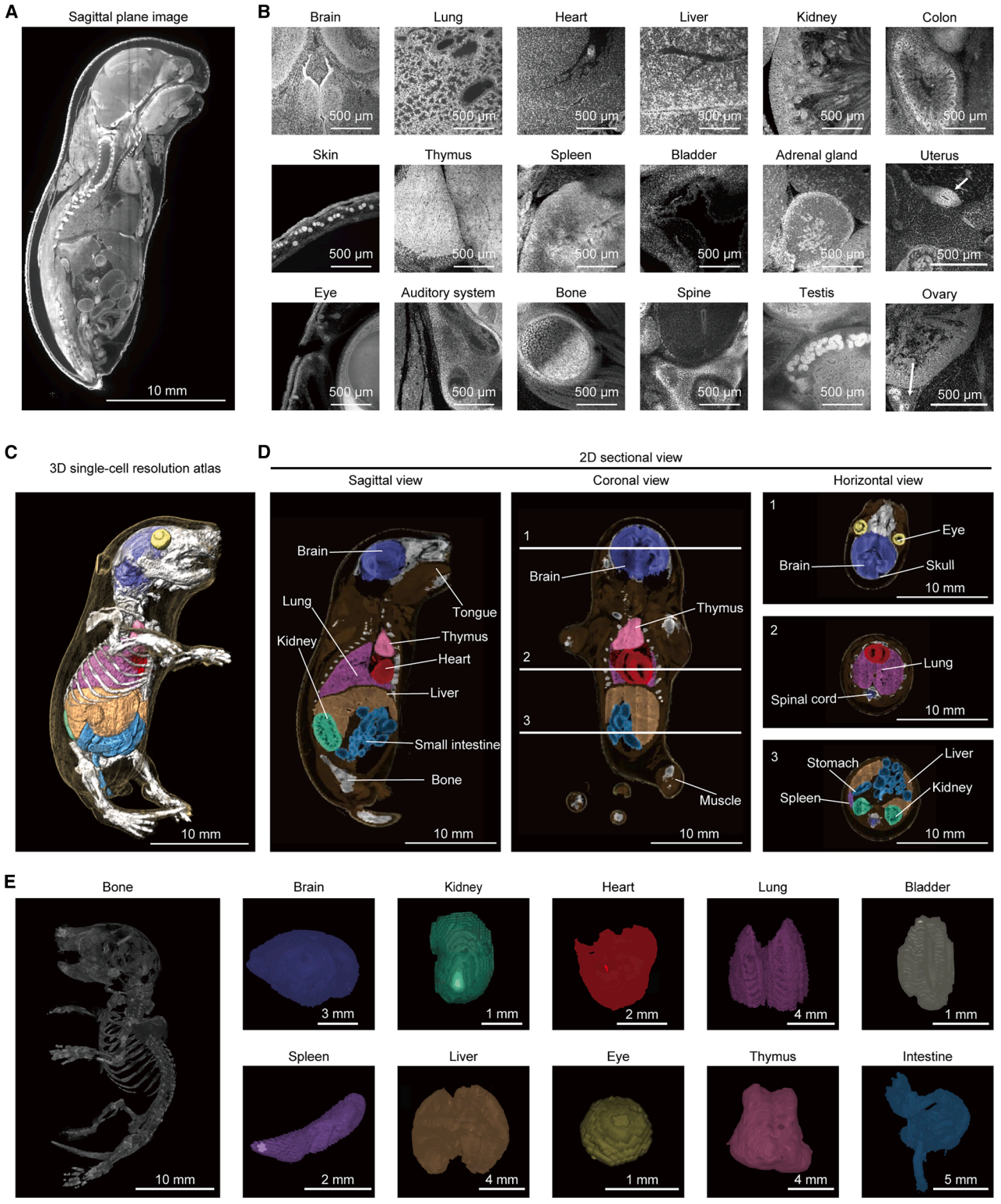

Figure 6. Construction of a single-cell-resolution atlas of the newborn mouse body (CUBIC Body Atlas)

(A) Sagittal-plane image of a nuclear-stained C57BL/6N male P0 mouse.

(B) High-resolution images of various organs across the whole body.

(legend continued on next page)

assess segmentation accuracy (Figure S6G). This annotation allowed individual organs to be digitally extracted from the atlas (Figure 6E).

The CUBIC Body Atlas enables whole-body single-cell profiling of multiple samples

We conducted cellome-wide analyses across the whole body using the same framework as the CUBIC Organ Atlas (Figure 7A). As an initial application, we quantified total cell numbers and densities for each annotated anatomical region. To this end, whole-body single-cell-resolution datasets from two additional male specimens (not used for atlas construction) were registered to the CUBIC Body Atlas. Registration accuracy was evaluated by overlaying the atlas images with the registered samples, showing good correspondence (Figures S6H and S6I). We then quantified total cell numbers and densities for each segmented organ in male mice ($n = 3$, including the atlas dataset) (Figure 7B). For example, the brain contained $4.87 \times 10^7 \pm 1.01 \times 10^6$ cells. All values are provided in Table S1. We also registered whole-body datasets from three female specimens to the CUBIC Body Atlas. After manually segmenting the uterus and ovaries, total cell numbers and densities were quantified for each segmented organ in female mice ($n = 3$) (Figure 7C).

Subsequently, we profiled a specific cell type using whole-body immunostaining. We focused on macrophages, which are essential for early immune responses, tissue repair, and homeostasis,[70,71] yet whose total numbers and whole-body distribution remain poorly understood. To map their whole-body distribution, we performed whole-body immunostaining with anti-IBA1 ($n = 3$), which labels macrophages, dendritic cells, and monocytes. Because IBA1-positive cells are sparsely distributed relative to nuclei, we acquired images using lower-resolution LSFM (voxel size: 10 μm × 10 μm × 10 μm). The data revealed IBA1-positive cells and their clusters throughout the body (Figure S7). The IBA1-positive cells were then detected, and their coordinates were extracted (Figure 7D). Detection performance reached a TPR of 88%–97% and a PPV of 87%–97% (Figure S2R). Nuclear-stained images acquired in parallel were registered to the CUBIC Body Atlas, and the resulting transformation was applied to the IBA1-positive cell coordinates, enabling whole-body mapping of their distribution (Figures 7E and 7F). We next quantified IBA1-positive cell numbers and densities across annotated organs (Figure 7G). The cell numbers ranged from $1.30 \times 10^3 \pm 5.62 \times 10^2$ (bladder) to $1.99 \times 10^5 \pm 2.81 \times 10^4$ (bone). Next, we computed nearest-neighbor distances for IBA1-positive cells in each organ and visualized their distributions as histograms (Figures 7H and 7I). In the brain, IBA1-positive cells showed a narrow distance distribution with small intercellular distances, consistent with previous reports that microglia are uniformly and densely distributed[72] In contrast, the lungs exhibited a broader distribution, consistent with previous reports that they contain both high density and low-density macrophage populations.[73] These observations suggest a close relationship between the distribution patterns of IBA1-positive cells and the organ structure.

In addition, we analyzed the 3D distribution of α-SMA-positive and tyrosine hydroxylase (TH)-positive structures in the whole-body dataset ($n = 1$), further demonstrating the applicability of the CUBIC Body Atlas for vascular and neuronal mapping (Figures 7J and 7K).

Taken together, we successfully demonstrated that the CUBIC Organ/Body Atlas was applicable to the whole-organ/-body single-cell-resolution analysis. As a resource for the scientific community, these atlas datasets are available on the website (https://whole.cfosdb.systems-based-medicine.org/whole_body/). Like other omics platforms, this cellomics resource supports user-driven applications. To improve accessibility, we developed an interactive web interface that allows cross-sectional exploration of the CUBIC Organ/Body Atlas. Downloadable CSV files containing point cloud coordinates with anatomical region IDs further enable researchers to integrate their own datasets.

DISCUSSION

Organ- and body-wide cell detection enabled by exMOVIE light-sheet microscopy

Quantifying cell numbers within organs and across the whole body has long been a central question in anatomy. Previous estimates relied on sampling-based counts,[74,75] and only recently have whole-organ cell counts been reported for the mouse brain.[39,42] Here, we achieved the detection and enumeration of all cells in major organs and an entire mammalian body. These values were consistent with independent estimates derived from organ DNA content. Using reported organ weight/DNA weight ratios[76] and our prior brain cell counts[39], DNA-based estimates for the kidney (7.96×10^7) and liver (2.71×10^8) differed by less than 10% from our directly measured values (7.17×10^7 and 2.94×10^8), supporting the accuracy of our measurements.

Constructing the CUBIC Organ/Body Atlas required developing the exMOVIE system for single-cell-resolution imaging of whole organs and the entire body. exMOVIE provided two key advantages. First, it overcame the resolution-working distance trade-off[77] by adopting a 10×/NA 0.3/WD 30-mm objective, allowing high-resolution imaging of specimens far thicker than those accessible with conventional 10×/NA 0.6/WD 8-mm lenses. Second, the improved axial resolution of exMOVIE (5 μm FWHM, compared with approximately 11 μm for the microscope used to image CUBIC-X-expanded brain tissue) eliminated the need for the approximately 10-fold tissue expansion required by the CUBIC-X protocol[42]. In this study, a more moderate, approximately 3-fold expansion using CUBIC-R+ was sufficient for single-cell imaging across diverse organs, substantially reducing imaging time and data volume while maintaining reliable cell detection. These advances collectively enabled the construction of the CUBIC Organ/Body Atlas, providing a foundational reference for organ- and body-wide cellomics.

(C) 3D single-cell-resolution atlas of the P0 mouse body.
(D) 2D single-cell-resolution atlas of the P0 mouse body, showing sagittal (left), coronal (middle), and horizontal (right) views with detailed labeling.
(E) 3D cell density images of individual organs derived from the CUBIC Body Atlas.
See also Figures S2, S3, and S6.

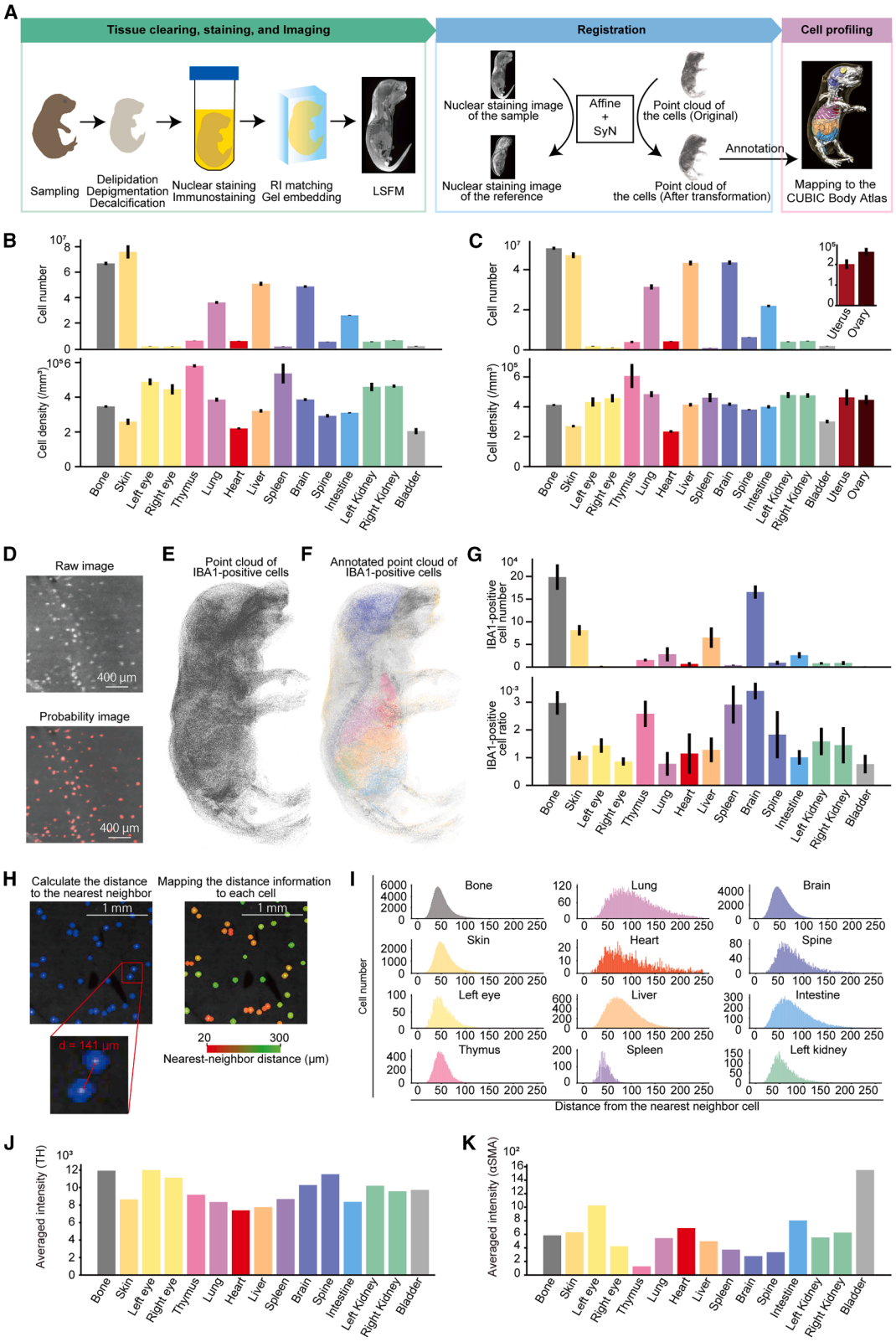

(legend on next page)

The CUBIC Organ/Body Atlas enables whole-organ/-body comparative analysis in development, pathology, and physiology

The CUBIC Organ/Body Atlas provides a 3D point cloud of all cells within each organ, enabling quantitative multi-sample comparisons. In kidney development, this atlas-based cellome analysis captured region-specific changes in cell number, volume, and density across post-natal stages. Medullary cell numbers plateaued by week 3, consistent with transcriptomic studies of nephrogenesis.[78] Layer-based analysis of the medulla revealed three spatially organized developmental clusters, highlighting 3D heterogeneity that cannot be detected from 2D histology. In pathology, analysis of cisplatin-treated kidneys revealed global cell loss with pronounced reductions in the cortex, extending classical findings of proximal tubular injury[79] to an organ-wide context. In LPS-induced lung inflammation, we observed phenomena consistent with prior reports that LPS drives immune cell recruitment[80]; however, our analysis provided a whole-organ, single-cell-resolution view revealing that these increases were concentrated within the cell-enriched area. Using CUBIC Body Atlas, we quantified systemic distributions of IBA1-positive macrophages. This revealed organ-to-organ variability in abundance and spatial patterns. This framework can be extended to additional markers, allowing integration of molecularly defined cell types into the atlas.

Future perspective

Several 3D organ and whole-body atlases and datasets have been developed, including the Allen Brain Atlas,[47] wildDISCO,[81] and iDISCO+,[21] each offering distinct strengths in resolution, labeling strategies, and anatomical coverage (Table S2). The CUBIC Organ/Body Atlas complements, rather than competes with, existing frameworks by providing a single-cell-resolution "white map" onto which diverse datasets can be integrated.

The CUBIC Organ/Body Atlas is currently provided as a 3D point cloud composed solely of spatial coordinates of cells or with minimal anatomical region information. Adding information such as cell types and cell-cell interactions is crucial, particularly for ensuring interoperability with whole-body cell atlases such as the Human Cell Atlas[82] and *Tabula Muris*.[83] Achieving higher molecular multiplexing in 3D tissues remains technically challenging, but an ultra-multicolor staining method and the utilization of wider wavelength ranges will support addressing this challenge.[13,84] As dataset sizes grow with increasing resolution, our computational pipeline is designed to scale through GPU expansion, CPU upgrades, and cloud-based processing. Continued advances in efficient computation and AI-assisted feature extraction will be critical.[13] Moreover, ST integration represents a particularly promising direction. By mapping a published kidney ST section[85] onto the CUBIC Organ/Body Atlas, we demonstrate the feasibility of multimodal alignment between molecular and spatial coordinates (Figure S6J). As 3D ST datasets become available, the atlas may serve as a structural scaffold for unifying transcriptomic, anatomical, and cell-type information. In addition, alongside the growing accessibility of open-source LSFM platforms such as mesoSPIM[86,87] and deScSPIM,[88] these developments will broaden the range of applications supported by the atlas and strengthen its role as a central reference for spatial cellomics.

Limitations of the study

Systematic quantitative analysis of whole-body immunostaining was performed only for IBA1-positive cells, whereas other markers (TH and α-SMA) were examined only in pilot datasets. Broader cell-type profiling will require additional markers. Although most BABB-cleared samples were compatible with the atlas, the left atrium could not be accurately registered (Figures 7J and 7K), indicating that shape changes from clearing methods must be considered when integrating external datasets. When the atlas is applied using low-resolution LSFM, detection accuracy may decline in dense tissues. Appropriate selection of imaging resolution based on tissue characteristics and analytical goals is therefore essential to ensure reliable quantification. Moreover, although point cloud representation is advantageous for large-scale spatial analysis, it inherently lacks information such as detailed volume, morphology, and interactions. Incorporating additional biological attributes into the point cloud could enhance its utility for more structurally detailed analyses. Finally, anatomical variability across individuals can limit the precision of fine-scale alignment. For example, internal structures such as glomeruli and intestinal folds show substantial variation, making high-resolution alignment difficult even when overall organ registration is preserved (Figure S6I). Such variability imposes important constraints when applying the atlas to comparative studies focused on fine anatomical features.

RESOURCE AVAILABILITY

Lead contact

Further information and requests for resources and reagents should be directed to and will be fulfilled by the lead contact, Hiroki R. Ueda (uedah-tky@umin.ac.jp).

Figure 7. The CUBIC Body Atlas enables whole-body cell profiling

(A) Workflow for cell profiling in the P0 mouse body.
(B and C) Quantification of cell numbers (top) and cell densities (bottom) across various organs and tissues in the male (B) and female (C) mouse body (n = 3).
(D) Raw and probability images showing IBA1-positive cells in the brain.
(E and F) Point cloud (E) and annotated point cloud (F) of IBA1-positive cells across the entire mouse body.
(G) Quantification of IBA1-positive cell numbers (top) and IBA1-positive cell ratios (bottom) across various organs and tissues (n = 3).
(H) 3D nearest-neighbor analysis of IBA1-positive cells.
(I) Histograms of distances between IBA1-positive cells for each organ.
(J and K) Quantification of average intensities of TH (top) and α-SMA (bottom) across various organs and tissues (n = 1).
Error bars represent mean ± SD.
See also Figures S2, S6, and S7.

Materials availability

This study did not generate new, unique reagents.

Data and code availability

Generated data, including the atlas datasets, are available on our website (https://whole.cfosdb.systems-based-medicine.org/whole_body/). Visualization can also be performed using the tools provided on the site. All original code generated in this study has been deposited in Zenodo and is accessible under a permanent DOI (Zenodo: https://doi.org/10.5281/ZENODO.18028197).[89] The corresponding GitHub repository is available at https://github.com/OrganismalSystemsBiology/WholeOrganAtlas.

ACKNOWLEDGMENTS

We thank the people at RIKEN and the University of Tokyo, in particular R.G. Yamada, for helping with data analysis; H. Fujishima for helping with animal experiments; and S. Hasegawa for providing the expert opinion regarding kidney layer structure. This work was supported by a JST ERATO grant (H.R.U, no. JPMJER2001), a JST (Moonshot R&D) grant (K.M., no. JPMJMS2023), a MEXT Quantum Leap Flagship Program (MEXT QLEAP) grant (H.R.U., no. JPMXS0120330644), a JSPS KAKENHI grant-in-aid for scientific research (S) (H.R.U., no. JP18H05270), a JSPS KAKENHI grant-in-aid for scientific research (C) (K.M., no. 20K06885), a JSPS KAKENHI grant-in-aid for Early-Career Scientists (S.Y.Y., no. 20K16626), a grant-in-aid from the Human Frontier Science Program (H.R.U.), the Science and Technology Platform Program for Advanced Biological Medicine (AMED/MEXT, H.R.U.), a JSPS KAKENHI grant-in-aid for scientific research (B) (E.M., no. 23K27391), AMED grants (S.T., no. JP22cm0106286 and JP24ama221220), the Japan Agency for Medical Research and Development (AMED)-Project for Promotion of Cancer Research and Therapeutic Evolution (P-PROMOTE) (E.A.S., JP22ama221517), AMED-Research on Development of New Drugs (E.A.S., JP21ak0101181), AMED-Brain/MINDS (E.A.S., JP21wm0425003), Japan Science and Technology Agency (JST)-CREST (E.A.S., JPMJCR23B7), Japan Society for the Promotion of Science (JSPS)-KAKENHI grant-in-aid for scientific research (B) (E.A.S., JP22H02824), JSPS-KAKENHI Grant-in-Aid for Transformative Research Areas - Platforms for Advanced Technologies and Research Resources "Advanced Bioimaging Support" (E.A.S., JP22H04926), JSPS-KAKENHI for International Leading Research (E.A.S., 23K20044), Grants-in-Aid from Nakatani foundation for advancement of measuring technologies in biomedical engineering (E.A.S.), The Uehara Memorial Foundation (E.A.S.), UTEC-UTokyo (E.A.S.), the Takeda Science Foundation (E.A.S.), and collaboration research funding with Kantum Ushikata Co., Ltd (E.A.S.).

AUTHOR CONTRIBUTIONS

S.Y.Y., K.M., and H.R.U. designed the study. S.Y.Y. and K.M. performed most of the experiments. S.Y.Y. performed most of the computational analyses. E.A.S. optimized the immunostaining protocol. S.T. established the pulmonary metastasis mouse model and performed imaging. D.S. developed the tissue clearing protocol for newborn mice. S.Y.Y., K.M., and E.A.S. wrote the manuscript with supervision from H.R.U. All authors discussed the results and commented on the manuscript.

DECLARATION OF INTERESTS

K.M., E.A.S., and H.R.U. are inventors on patents and patent applications owned by RIKEN and CUBICStars Inc. covering the CUBIC tissue clearing and staining reagents and the MOVIE system. H.R.U., K.M., and E.A.S. are side workers at CUBICStars Inc. and hold shares in the company. S.Y.Y. is a side worker at CUBICStars Inc. E.A.S. has received collaboration funding from Kantum Ushikata Co., Ltd.

DECLARATION OF GENERATIVE AI AND AI-ASSISTED TECHNOLOGIES IN THE WRITING PROCESS

During the preparation of this work, the authors used ChatGPT in order to improve language and readability. After using this tool, the authors reviewed and edited the content as needed and take full responsibility for the content of the publication.

STAR★METHODS

Detailed methods are provided in the online version of this paper and include the following:

- KEY RESOURCES TABLE
- EXPERIMENTAL MODEL AND STUDY PARTICIPANT DETAILS
  - Animals
  - Cell lines
- METHOD DETAILS
  - Tissue clearing and staining of adult mouse organs using the CUBIC protocol
  - Tissue Clearing, Nuclear Staining, and Immunostaining of Neonatal Mice
  - Tissue Clearing of Adult Mouse Organs Using the BABB Protocol
  - Volume Correction using MRI data
  - Construction of a Customized Light-Sheet Microscope
  - Three-Dimensional Imaging of Whole Organs and the Entire Body at Cellular Resolution
  - Three-Dimensional Imaging of Lungs with Metastasized Tumor Cells Expressing ZsGreen and Whole-Body Immunostained Neonatal Mice
  - Experimental design and reporting considerations
- QUANTIFICATION AND STATISTICAL ANALYSIS
  - Nuclear Detection
  - Detection of IBA1-Positive Cells
  - Stitching and alignment of large organ-wide 3D image stacks
  - Calculation of Organ Volume and Cell Density in Mice
  - Segmentation and Creation of the CUBIC Organ/Body Atlas
  - Mapping and Annotation to the CUBIC Organ/Body Atlas
  - Whole-kidney cell-profiling of mice at different ages
  - Statistical Analysis
  - Computational Requirements for Atlas Processing
- ADDITIONAL RESOURCES

SUPPLEMENTAL INFORMATION

Supplemental information can be found online at https://doi.org/10.1016/j.cell.2025.12.057.

Received: October 21, 2024
Revised: September 1, 2025
Accepted: December 30, 2025
Published: February 25, 2026

REFERENCES

1. Zeng, H. (2022). What is a cell type and how to define it? Cell *185*, 2739–2755. https://doi.org/10.1016/j.cell.2022.06.031.
2. Gómez-Gaviro, M.V., Sanderson, D., Ripoll, J., and Desco, M. (2020). Biomedical Applications of Tissue Clearing and Three-Dimensional Imaging in Health and Disease. iScience *23*, 101432. https://doi.org/10.1016/j.isci.2020.101432.
3. Nojima, S., Susaki, E.A., Yoshida, K., Takemoto, H., Tsujimura, N., Iijima, S., Takachi, K., Nakahara, Y., Tahara, S., Ohshima, K., et al. (2017). CUBIC pathology: three-dimensional imaging for pathological diagnosis. Sci. Rep. *7*, 9269. https://doi.org/10.1038/s41598-017-09117-0.
4. Song, A.H., Williams, M., Williamson, D.F.K., Chow, S.S.L., Jaume, G., Gao, G., Zhang, A., Chen, B., Baras, A.S., Serafin, R., et al. (2024). Analysis of 3D pathology samples using weakly supervised AI. Cell *187*, 2502–2520.e17. https://doi.org/10.1016/j.cell.2024.03.035.
5. Vogelstein, B., Lane, D., and Levine, A.J. (2000). Surfing the p53 network. Nature *408*, 307–310. https://doi.org/10.1038/35042675.

6. Butt, D., Chan, T.D., Bourne, K., Hermes, J.R., Nguyen, A., Statham, A., O'Reilly, L.A., Strasser, A., Price, S., Schofield, P., et al. (2015). FAS inactivation releases unconventional germinal center B cells that escape antigen control and drive IgE and autoantibody production. Immunity *42*, 890–902. https://doi.org/10.1016/j.immuni.2015.04.010.

7. Ilieva, H., Polymenidou, M., and Cleveland, D.W. (2009). Non-cell autonomous toxicity in neurodegenerative disorders: ALS and beyond. J. Cell Biol. *187*, 761–772. https://doi.org/10.1083/jcb.200908164.

8. Xu, Y., Wang, S., Feng, Q., Xia, J., Li, Y., Li, H.-D., and Wang, J. (2024). scCAD: Cluster decomposition-based anomaly detection for rare cell identification in single-cell expression data. Nat. Commun. *15*, 7561. https://doi.org/10.1038/s41467-024-51891-9.

9. Piwecka, M., Rajewsky, N., and Rybak-Wolf, A. (2023). Single-cell and spatial transcriptomics: deciphering brain complexity in health and disease. Nat. Rev. Neurol. *19*, 346–362. https://doi.org/10.1038/s41582-023-00809-y.

10. Tian, L., Chen, F., and Macosko, E.Z. (2023). The expanding vistas of spatial transcriptomics. Nat. Biotechnol. *41*, 773–782. https://doi.org/10.1038/s41587-022-01448-2.

11. Bressan, D., Battistoni, G., and Hannon, G.J. (2023). The dawn of spatial omics. Science *381*, eabq4964. https://doi.org/10.1126/science.abq4964.

12. Prabhakaran, S. (2022). Sparcle: assigning transcripts to cells in multiplexed images. Bioinform. Adv. *2*, vbac048. https://doi.org/10.1093/bioadv/vbac048.

13. Ertürk, A. (2024). Deep 3D histology powered by tissue clearing, omics and AI. Nat. Methods *21*, 1153–1165. https://doi.org/10.1038/s41592-024-02327-1.

14. Mitani, T.T., Susaki, E.A., Matsumoto, K., and Ueda, H.R. (2024). Realization of cellomics to dive into the whole-body or whole-organ cell cloud. Nat. Methods *21*, 1138–1142. https://doi.org/10.1038/s41592-024-02307-5.

15. Yang, B., Treweek, J.B., Kulkarni, R.P., Deverman, B.E., Chen, C.-K., Lubeck, E., Shah, S., Cai, L., and Gradinaru, V. (2014). Single-Cell Phenotyping within Transparent Intact Tissue through Whole-Body Clearing. Cell *158*, 945–958. https://doi.org/10.1016/j.cell.2014.07.017.

16. Pan, C., Cai, R., Quacquarelli, F.P., Ghasemigharagoz, A., Lourbopoulos, A., Matryba, P., Plesnila, N., Dichgans, M., Hellal, F., and Ertürk, A. (2016). Shrinkage-mediated imaging of entire organs and organisms using uDISCO. Nat. Methods *13*, 859–867. https://doi.org/10.1038/nmeth.3964.

17. Park, Y.-G., Sohn, C.H., Chen, R., McCue, M., Yun, D.H., Drummond, G.T., Ku, T., Evans, N.B., Oak, H.C., Trieu, W., et al. (2018). Protection of tissue physicochemical properties using polyfunctional crosslinkers. Nat. Biotechnol. *37*, 73–83. https://doi.org/10.1038/nbt.4281.

18. Voie, A.H., Burns, D.H., and Spelman, F.A. (1993). Orthogonal-plane fluorescence optical sectioning: three-dimensional imaging of macroscopic biological specimens. J. Microsc. *170*, 229–236. https://doi.org/10.1111/j.1365-2818.1993.tb03346.x.

19. Dodt, H.-U., Leischner, U., Schierloh, A., Jährling, N., Mauch, C.P., Deininger, K., Deussing, J.M., Eder, M., Zieglgänsberger, W., and Becker, K. (2007). Ultramicroscopy: three-dimensional visualization of neuronal networks in the whole mouse brain. Nat. Methods *4*, 331–336. https://doi.org/10.1038/nmeth1036.

20. Hama, H., Kurokawa, H., Kawano, H., Ando, R., Shimogori, T., Noda, H., Fukami, K., Sakaue-Sawano, A., and Miyawaki, A. (2011). Scale: a chemical approach for fluorescence imaging and reconstruction of transparent mouse brain. Nat. Neurosci. *14*, 1481–1488. https://doi.org/10.1038/nn.2928.

21. Renier, N., Adams, E.L., Kirst, C., Wu, Z., Azevedo, R., Kohl, J., Autry, A.E., Kadiri, L., Umadevi Venkataraju, K., Zhou, Y., et al. (2016). Mapping of Brain Activity by Automated Volume Analysis of Immediate Early Genes. Cell *165*, 1789–1802. https://doi.org/10.1016/j.cell.2016.05.007.

22. Vieites-Prado, A., and Renier, N. (2021). Tissue clearing and 3D imaging in developmental biology. Development *148*, dev199369. https://doi.org/10.1242/dev.199369.

23. Almagro, J., Messal, H.A., Zaw Thin, M., van Rheenen, J., and Behrens, A. (2021). Tissue clearing to examine tumour complexity in three dimensions. Nat. Rev. Cancer *21*, 718–730. https://doi.org/10.1038/s41568-021-00382-w.

24. Roostalu, U., Hansen, H.H., and Hecksher-Sørensen, J. (2024). 3D light-sheet fluorescence microscopy in preclinical and clinical drug discovery. Drug Discov. Today *29*, 104196. https://doi.org/10.1016/j.drudis.2024.104196.

25. Ueda, H.R., Ertürk, A., Chung, K., Gradinaru, V., Chédotal, A., Tomancak, P., and Keller, P.J. (2020). Tissue clearing and its applications in neuroscience. Nat. Rev. Neurosci. *21*, 61–79. https://doi.org/10.1038/s41583-019-0250-1.

26. Richardson, D.S., Guan, W., Matsumoto, K., Pan, C., Chung, K., Ertürk, A., Ueda, H.R., and Lichtman, J.W. (2021). Tissue clearing. Nat. Rev. Methods Primers *1*, 84.

27. Becker, K., Jährling, N., Kramer, E.R., Schnorrer, F., and Dodt, H.U. (2008). Ultramicroscopy: 3D reconstruction of large microscopical specimens. J. Biophotonics *1*, 36–42. https://doi.org/10.1002/jbio.200710011.

28. Ertürk, A., Becker, K., Jährling, N., Mauch, C.P., Hojer, C.D., Egen, J.G., Hellal, F., Bradke, F., Sheng, M., and Dodt, H.-U. (2012). Three-dimensional imaging of solvent-cleared organs using 3DISCO. Nat. Protoc. *7*, 1983–1995. https://doi.org/10.1038/nprot.2012.119.

29. Susaki, E.A., Tainaka, K., Perrin, D., Kishino, F., Tawara, T., Watanabe, T.M., Yokoyama, C., Onoe, H., Eguchi, M., Yamaguchi, S., et al. (2014). Whole-brain imaging with single-cell resolution using chemical cocktails and computational analysis. Cell *157*, 726–739. https://doi.org/10.1016/j.cell.2014.03.042.

30. Zhu, J., Yu, T., Li, Y., Xu, J., Qi, Y., Yao, Y., Ma, Y., Wan, P., Chen, Z., Li, X., et al. (2020). MACS: Rapid Aqueous Clearing System for 3D mapping of intact organs. Adv. Sci. (Weinh) *7*, 1903185. https://doi.org/10.1002/advs.201903185.

31. Chung, K., Wallace, J., Kim, S.-Y., Kalyanasundaram, S., Andalman, A.S., Davidson, T.J., Mirzabekov, J.J., Zalocusky, K.A., Mattis, J., Denisin, A.K., et al. (2013). Structural and molecular interrogation of intact biological systems. Nature *497*, 332–337. https://doi.org/10.1038/nature12107.

32. Glaser, A.K., Reder, N.P., Chen, Y., McCarty, E.F., Yin, C., Wei, L., Wang, Y., True, L.D., and Liu, J.T.C. (2017). Light-sheet microscopy for slide-free non-destructive pathology of large clinical specimens. Nat. Biomed. Eng. *1*, 0084. https://doi.org/10.1038/s41551-017-0084.

33. Ahrens, M.B., Orger, M.B., Robson, D.N., Li, J.M., and Keller, P.J. (2013). Whole-brain functional imaging at cellular resolution using light-sheet microscopy. Nat. Methods *10*, 413–420. https://doi.org/10.1038/nmeth.2434.

34. Keller, P.J., Schmidt, A.D., Wittbrodt, J., and Stelzer, E.H.K. (2008). Reconstruction of zebrafish early embryonic development by scanned light sheet microscopy. Science *322*, 1065–1069. https://doi.org/10.1126/science.1162493.

35. Silvestri, L., Bria, A., Sacconi, L., Iannello, G., and Pavone, F.S. (2012). Confocal light sheet microscopy: micron-scale neuroanatomy of the entire mouse brain. Opt. Express *20*, 20582–20598. https://doi.org/10.1364/OE.20.020582.

36. Silvestri, L., Müllenbroich, M.C., Costantini, I., Di Giovanna, A.P., Mazzamuto, G., Franceschini, A., Kutra, D., Kreshuk, A., Checcucci, C., Toresano, L.O., et al. (2021). Universal autofocus for quantitative volumetric microscopy of whole mouse brains. Nat. Methods *18*, 953–958. https://doi.org/10.1038/s41592-021-01208-1.

37. Gao, L. (2015). Extend the field of view of selective plan illumination microscopy by tiling the excitation light sheet. Opt. Express *23*, 6102–6111. https://doi.org/10.1364/OE.23.006102.

38. Dean, K.M., Chakraborty, T., Daetwyler, S., Lin, J., Garrelts, G., M'Saad, O., Mekbib, H.T., Voigt, F.F., Schaettin, M., Stoeckli, E.T., et al. (2022).

Isotropic imaging across spatial scales with axially swept light-sheet microscopy. Nat. Protoc. *17*, 2025–2053. https://doi.org/10.1038/s41596-022-00706-6.

39. Matsumoto, K., Mitani, T.T., Horiguchi, S.A., Kaneshiro, J., Murakami, T.C., Mano, T., Fujishima, H., Konno, A., Watanabe, T.M., Hirai, H., et al. (2019). Advanced CUBIC tissue clearing for whole-organ cell profiling. Nat. Protoc. *14*, 3506–3537. https://doi.org/10.1038/s41596-019-0240-9.
40. Glaser, A., Chandrashekar, J., Vasquez, S., Arshadi, C., Ouellette, N., Jiang, X., Baka, J., Kovacs, G., Woodard, M., Seshamani, S., et al. (2024). Expansion-assisted selective plane illumination microscopy for nanoscale imaging of centimeter-scale tissues. eLife *12*, RP91979. https://doi.org/10.7554/eLife.91979.
41. Roy, D.S., Park, Y.-G., Kim, M.E., Zhang, Y., Ogawa, S.K., DiNapoli, N., Gu, X., Cho, J.H., Choi, H., Kamentsky, L., et al. (2022). Brain-wide mapping reveals that engrams for a single memory are distributed across multiple brain regions. Nat. Commun. *13*, 1799. https://doi.org/10.1038/s41467-022-29384-4.
42. Murakami, T.C., Mano, T., Saikawa, S., Horiguchi, S.A., Shigeta, D., Baba, K., Sekiya, H., Shimizu, Y., Tanaka, K.F., Kiyonari, H., et al. (2018). A three-dimensional single-cell-resolution whole-brain atlas using CUBIC-X expansion microscopy and tissue clearing. Nat. Neurosci. *21*, 625–637. https://doi.org/10.1038/s41593-018-0109-1.
43. Mano, T., Murata, K., Kon, K., Shimizu, C., Ono, H., Shi, S., Yamada, R.G., Miyamichi, K., Susaki, E.A., Touhara, K., et al. (2021). CUBIC-Cloud provides an integrative computational framework toward community-driven whole-mouse-brain mapping. Cell Rep. Methods *1*, 100038. https://doi.org/10.1016/j.crmeth.2021.100038.
44. Stefaniuk, M., Pawłowska, M., Barański, M., Nowicka, K., Zieliński, Z., Bijoch, Ł., Legutko, D., Majka, P., Bednarek, S., Jermakow, N., et al. (2023). Global brain c-Fos profiling reveals major functional brain networks rearrangements after alcohol reexposure. Neurobiol. Dis. *178*, 106006. https://doi.org/10.1016/j.nbd.2023.106006.
45. Hansen, H.H., Perens, J., Roostalu, U., Skytte, J.L., Salinas, C.G., Barkholt, P., Thorbek, D.D., Rigbolt, K.T.G., Vrang, N., Jelsing, J., et al. (2021). Whole-brain activation signatures of weight-lowering drugs. Mol. Metab. *47*, 101171. https://doi.org/10.1016/j.molmet.2021.101171.
46. Franceschini, A., Mazzamuto, G., Checcucci, C., Chicchi, L., Fanelli, D., Costantini, I., Passani, M.B., Silva, B.A., Pavone, F.S., and Silvestri, L. (2023). Brain-wide neuron quantification toolkit reveals strong sexual dimorphism in the evolution of fear memory. Cell Rep. *42*, 112908. https://doi.org/10.1016/j.celrep.2023.112908.
47. Wang, Q., Ding, S.-L., Li, Y., Royall, J., Feng, D., Lesnar, P., Graddis, N., Naeemi, M., Facer, B., Ho, A., et al. (2020). The Allen Mouse Brain Common Coordinate Framework: A 3D Reference Atlas. Cell *181*, 936–953.e20. https://doi.org/10.1016/j.cell.2020.04.007.
48. Blain, R., Couly, G., Shotar, E., Blévinal, J., Toupin, M., Favre, A., Abjaghou, A., Inoue, M., Hernández-Garzón, E., Clarençon, F., et al. (2023). A tridimensional atlas of the developing human head. Cell *186*, 5910–5924.e17. https://doi.org/10.1016/j.cell.2023.11.013.
49. Tainaka, K., Murakami, T.C., Susaki, E.A., Shimizu, C., Saito, R., Takahashi, K., Hayashi-Takagi, A., Sekiya, H., Arima, Y., Nojima, S., et al. (2018). Chemical Landscape for Tissue Clearing Based on Hydrophilic Reagents. Cell Rep. *24*, 2196–2210.e9. https://doi.org/10.1016/j.celrep.2018.07.056.
50. Susaki, E.A., Shimizu, C., Kuno, A., Tainaka, K., Li, X., Nishi, K., Morishima, K., Ono, H., Ode, K.L., Saeki, Y., et al. (2020). Versatile whole-organ/body staining and imaging based on electrolyte-gel properties of biological tissues. Nat. Commun. *11*, 1982. https://doi.org/10.1038/s41467-020-15906-5.
51. Hörl, D., Rojas Rusak, F., Preusser, F., Tillberg, P., Randel, N., Chhetri, R.K., Cardona, A., Keller, P.J., Harz, H., Leonhardt, H., et al. (2019). BigStitcher: reconstructing high-resolution image datasets of cleared and expanded samples. Nat. Methods *16*, 870–874. https://doi.org/10.1038/s41592-019-0501-0.
52. Bria, A., and Iannello, G. (2012). TeraStitcher - a tool for fast automatic 3D-stitching of teravoxel-sized microscopy images. BMC Bioinform. *13*, 316. https://doi.org/10.1186/1471-2105-13-316.
53. Pienn, M., Burgard, C., Payer, C., Avian, A., Urschler, M., Stollberger, R., Olschewski, A., Olschewski, H., Johnson, T., Meinel, F.G., et al. (2018). Healthy lung vessel morphology derived from thoracic computed tomography. Front. Physiol. *9*, 346. https://doi.org/10.3389/fphys.2018.00346.
54. Lorente, S., Hautefeuille, M., and Sanchez-Cedillo, A. (2020). The liver, a functionalized vascular structure. Sci. Rep. *10*, 16194. https://doi.org/10.1038/s41598-020-73208-8.
55. Lara, N. de L.E.M., Costa, G.M.J., Figueiredo, A.F.A., and de França, L.R. (2020). The Sertoli cell: what can we learn from different vertebrate models? Anim. Reprod. *16*, 81–92. https://doi.org/10.21451/1984-3143-AR2018-125.
56. Fedorov, A., Beichel, R., Kalpathy-Cramer, J., Finet, J., Fillion-Robin, J.-C., Pujol, S., Bauer, C., Jennings, D., Fennessy, F., Sonka, M., et al. (2012). 3D Slicer as an image computing platform for the Quantitative Imaging Network. Magn. Reson. Imaging *30*, 1323–1341. https://doi.org/10.1016/j.mri.2012.05.001.
57. Young, D.M., Fazel Darbandi, S., Schwartz, G., Bonzell, Z., Yuruk, D., Nojima, M., Gole, L.C., Rubenstein, J.L., Yu, W., and Sanders, S.J. (2021). Constructing and optimizing 3D atlases from 2D data with application to the developing mouse brain. eLife *10*, e61408. https://doi.org/10.7554/eLife.61408.
58. Jensen, B., Chang, Y.H., Bamforth, S.D., Mohun, T., Sedmera, D., Bartos, M., and Anderson, R.H. (2024). The changing morphology of the ventricular walls of mouse and human with increasing gestation. J. Anat. *244*, 1040–1053. https://doi.org/10.1111/joa.14017.
59. Thiesse, J., Namati, E., Sieren, J.C., Smith, A.R., Reinhardt, J.M., Hoffman, E.A., and McLennan, G. (2010). Lung structure phenotype variation in inbred mouse strains revealed through in vivo micro-CT imaging. J. Appl. Physiol. (1985) *109*, 1960–1968. https://doi.org/10.1152/japplphysiol.01322.2009.
60. Fiebig, T., Boll, H., Figueiredo, G., Kerl, H.U., Nittka, S., Groden, C., Kramer, M., and Brockmann, M.A. (2012). Three-dimensional in vivo imaging of the murine liver: a micro-computed tomography-based anatomical study. PLoS One *7*, e31179. https://doi.org/10.1371/journal.pone.0031179.
61. Missbach-Guentner, J., Pinkert-Leetsch, D., Dullin, C., Ufartes, R., Hornung, D., Tampe, B., Zeisberg, M., and Alves, F. (2018). 3D virtual histology of murine kidneys -high resolution visualization of pathological alterations by micro computed tomography. Sci. Rep. *8*, 1407. https://doi.org/10.1038/s41598-018-19773-5.
62. Berman, M.N., Tupper, C., and Bhardwaj, A. (2024). Physiology, left ventricular function. In StatPearls (StatPearls Publishing).
63. Ganesan, S., Comstock, A.T., and Sajjan, U.S. (2013). Barrier function of airway tract epithelium. Tissue Barriers *1*, e24997. https://doi.org/10.4161/tisb.24997.
64. Lin, M.-H., Chen, J.-C., Tian, X., Lee, C.-M., Yu, I.-S., Lo, Y.-F., Uchida, S., Huang, C.-L., Chen, B.-C., and Cheng, C.-J. (2021). Impairment in renal medulla development underlies salt wasting in Clc-k2 channel deficiency. JCI Insight *6*, e151039. https://doi.org/10.1172/jci.insight.151039.
65. Yuan, H.T., Suri, C., Yancopoulos, G.D., and Woolf, A.S. (1999). Expression of angiopoietin-1, angiopoietin-2, and the Tie-2 receptor tyrosine kinase during mouse kidney maturation. J. Am. Soc. Nephrol. *10*, 1722–1736. https://doi.org/10.1681/ASN.V1081722.
66. Rabe, M., and Schaefer, F. (2016). Non-transgenic mouse models of kidney disease. Nephron *133*, 53–61. https://doi.org/10.1159/000445171.
67. Taguchi, T., Nazneen, A., Abid, M.R., and Razzaque, M.S. (2005). Cisplatin-associated nephrotoxicity and pathological events. Contrib. Nephrol. *148*, 107–121. https://doi.org/10.1159/000086055.
68. Lv, X., Lu, X., Zhu, J., and Wang, Q. (2020). Lipopolysaccharide-induced acute lung injury is associated with increased Ran-binding protein in

microtubule-organizing center (RanBPM) molecule expression and mitochondria-mediated apoptosis signaling pathway in a mouse model. Med. Sci. Monit. *26*, e923172. https://doi.org/10.12659/MSM.923172.

69. Takagi, S., Sasaki, Y., Koike, S., Takemoto, A., Seto, Y., Haraguchi, M., Ukaji, T., Kawaguchi, T., Sugawara, M., Saito, M., et al. (2021). Platelet-derived lysophosphatidic acid mediated LPAR1 activation as a therapeutic target for osteosarcoma metastasis. Oncogene *40*, 5548–5558. https://doi.org/10.1038/s41388-021-01956-6.
70. Mass, E., Nimmerjahn, F., Kierdorf, K., and Schlitzer, A. (2023). Tissue-specific macrophages: how they develop and choreograph tissue biology. Nat. Rev. Immunol. *23*, 563–579. https://doi.org/10.1038/s41577-023-00848-y.
71. Paludan, S.R., Pradeu, T., Masters, S.L., and Mogensen, T.H. (2021). Constitutive immune mechanisms: mediators of host defence and immune regulation. Nat. Rev. Immunol. *21*, 137–150. https://doi.org/10.1038/s41577-020-0391-5.
72. Dos Santos, S.E., Medeiros, M., Porfirio, J., Tavares, W., Pessôa, L., Grinberg, L., Leite, R.E.P., Ferretti-Rebustini, R.E.L., Suemoto, C.K., Filho, W.J., et al. (2020). Similar microglial cell densities across brain structures and mammalian species: Implications for brain tissue function. J. Neurosci. *40*, 4622–4643. https://doi.org/10.1523/JNEUROSCI.2339-19.2020.
73. Balestrieri, B., Granata, F., Loffredo, S., Petraroli, A., Scalia, G., Morabito, P., Cardamone, C., Varricchi, G., and Triggiani, M. (2021). Phenotypic and functional heterogeneity of low density and high-density human lung macrophages. Biomedicines *9*, 505. https://doi.org/10.3390/biomedicines9050505.
74. Falconer, D.S., Gauld, I.K., and Roberts, R.C. (1978). Cell numbers and cell sizes in organs of mice selected for large and small body size. Genet. Res. *31*, 287–301. https://doi.org/10.1017/S0016672300018061.
75. Sohlenius-Sternbeck, A.-K. (2006). Determination of the hepatocellularity number for human, dog, rabbit, rat and mouse livers from protein concentration measurements. Toxicol. In Vitro *20*, 1582–1586. https://doi.org/10.1016/j.tiv.2006.06.003.
76. Schmidt, E.E., and Schibler, U. (1995). Cell size regulation, a mechanism that controls cellular RNA accumulation: consequences on regulation of the ubiquitous transcription factors Oct1 and NF-Y and the liver-enriched transcription factor DBP. J. Cell Biol. *128*, 467–483. https://doi.org/10.1083/jcb.128.4.467.
77. Susaki, E.A., and Ueda, H.R. (2016). Whole-body and Whole-Organ Clearing and Imaging Techniques with Single-Cell Resolution: Toward Organism-Level Systems Biology in Mammals. Cell Chem. Biol. *23*, 137–157. https://doi.org/10.1016/j.chembiol.2015.11.009.
78. Little, M.H., Howden, S.E., Lawlor, K.T., and Vanslambrouck, J.M. (2022). Determining lineage relationships in kidney development and disease. Nat. Rev. Nephrol. *18*, 8–21. https://doi.org/10.1038/s41581-021-00485-5.
79. Vickers, A.E.M., Rose, K., Fisher, R., Saulnier, M., Sahota, P., and Bentley, P. (2004). Kidney slices of human and rat to characterize cisplatin-induced injury on cellular pathways and morphology. Toxicol. Pathol. *32*, 577–590. https://doi.org/10.1080/01926230490508821.
80. Matute-Bello, G., Frevert, C.W., and Martin, T.R. (2008). Animal models of acute lung injury. Am. J. Physiol., Lung Cell. Mol. Physiol. *295*, L379–L399. https://doi.org/10.1152/ajplung.00010.2008.
81. Mai, H., Luo, J., Hoeher, L., Al-Maskari, R., Horvath, I., Chen, Y., Kofler, F., Piraud, M., Paetzold, J.C., Modamio, J., et al. (2024). Whole-body cellular mapping in mouse using standard IgG antibodies. Nat. Biotechnol. *42*, 617–627. https://doi.org/10.1038/s41587-023-01846-0.
82. Regev, A., Teichmann, S.A., Lander, E.S., Amit, I., Benoist, C., Birney, E., Bodenmiller, B., Campbell, P., Carninci, P., Clatworthy, M., et al. (2017). The Human Cell Atlas. eLife *6*, e27041. https://doi.org/10.7554/eLife.27041.
83. Tabula Muris Consortium (2018). Single-cell transcriptomics of 20 mouse organs creates a Tabula Muris. Nature *562*, 367–372. https://doi.org/10.1038/s41586-018-0590-4.
84. Susaki, E.A. (2024). Unlocking the potential of large-scale 3D imaging with tissue clearing techniques. Microscopy (Oxf.) *74*, 179–188.
85. Wu, H., Dixon, E.E., Xuanyuan, Q., Guo, J., Yoshimura, Y., Debashish, C., Niesnerova, A., Xu, H., Rouault, M., and Humphreys, B.D. (2024). High resolution spatial profiling of kidney injury and repair using RNA hybridization-based in situ sequencing. Nat. Commun. *15*, 1396. https://doi.org/10.1038/s41467-024-45752-8.
86. Voigt, F.F., Kirschenbaum, D., Platonova, E., Pagès, S., Campbell, R.A.A., Kastli, R., Schaettin, M., Egolf, L., van der Bourg, A., Bethge, P., et al. (2019). The mesoSPIM initiative: open-source light-sheet microscopes for imaging cleared tissue. Nat. Methods *16*, 1105–1108. https://doi.org/10.1038/s41592-019-0554-0.
87. Vladimirov, N., Voigt, F.F., Naert, T., Araujo, G.R., Cai, R., Reuss, A.M., Zhao, S., Schmid, P., Hildebrand, S., Schaettin, M., et al. (2024). Benchtop mesoSPIM: a next-generation open-source light-sheet microscope for cleared samples. Nat. Commun. *15*, 2679. https://doi.org/10.1038/s41467-024-46770-2.
88. Otomo, K., Omura, T., Nozawa, Y., Edwards, S.J., Sato, Y., Saito, Y., Yagishita, S., Uchida, H., Watakabe, Y., Naitou, K., et al. (2024). descSPIM: an affordable and easy-to-build light-sheet microscope optimized for tissue clearing techniques. Nat. Commun. *15*, 4941. https://doi.org/10.1038/s41467-024-49131-1.
89. Matsumoto, K. (2025). OrganismalSystemsBiology/WholeOrganAtlas: Whole-organ_Atlas. Zenodo. https://doi.org/10.5281/ZENODO.18028197.
90. Chen, C.-L., Liao, J.-W., Hu, O.Y.-P., and Pao, L.-H. (2016). Blockade of KCa3.1 potassium channels protects against cisplatin-induced acute kidney injury. Arch. Toxicol. *90*, 2249–2260. https://doi.org/10.1007/s00204-015-1607-5.
91. Ehrentraut, H., Weisheit, C., Scheck, M., Frede, S., and Hilbert, T. (2018). Experimental murine acute lung injury induces increase of pulmonary TIE2-expressing macrophages. J. Inflamm. (Lond) *15*, 12. https://doi.org/10.1186/s12950-018-0188-5.
92. Akiyama, F., Matsumoto, K., Yamashita, K., Oishi, A., Kitaoka, T., and Ueda, H.R. (2025). A multiwell plate approach to increase the sample throughput during tissue clearing. Nat. Protoc. *20*, 967–988. https://doi.org/10.1038/s41596-024-01080-1.

STAR★METHODS

KEY RESOURCES TABLE

REAGENT or RESOURCE	SOURCE	IDENTIFIER
Antibodies		
α-Smooth Muscle Actin	Sigma-Aldrich	A5228; RRID:AB_262054
Mouse IgG2a	Jackson Immuno Research	115-587-186; RRID:AB_2632540
IBA1	Abcam	ab178847; RRID:AB_2832244
Tyrosine Hydroxylase	Abcam	ab137869; RRID:AB_2801410
Rabbit IgG	Jackson Immuno Research	111-587-008; RRID:AB_2632469
Biological samples		
C57BL/6NJcl mice	CLEA Japan, Inc.	C57BL/6NJcl; RRID:MGI:2160139
SCID-beige mice	Charles River Laboratories	CB17.Cg-Prkdc^{scid}Lyst^{bg-J}/ CrlCrlj
Chemicals, peptides, and recombinant proteins		
paraformaldehyde	Nacalai Tesque	02890-45; CAS 30525-89-4
cisplatin	Fujifilm	033-20091; CAS 15663-27-1
medetomidine	Orion Corporation	Domitor®; CAS 86347-15-1
midazolam	Astellas Pharma Inc.	Dormicum®; CAS 59467-70-8
butorphanol	Meiji Animal Health Co., Ltd.	Vetorphale®; CAS 42408-82-2
LPS	Sigma-Aldrich	L2880; CAS 93572-42-0
ONO-7300243	Cayman Chemical Company	22052; CAS 638132-34-0
Propidium iodide	Life Technologies	P21493; CAS 25535-16-4
N-butyldiethanolamine	TOKYO CHEMICAL INDUSTRY CO., LTD.	B0725; CAS 102-79-4
Triton X-100	Nacalai Tesque	12967-45; CAS 9036-19-5
antipyrine	TOKYO CHEMICAL INDUSTRY CO., LTD.	D1876; CAS 60-80-0
nicotinamide	TOKYO CHEMICAL INDUSTRY CO., LTD.	N0078; CAS 98-92-0
casein	FUJIFILM Wako	#030-01505; CAS 91079-40-2
hydrogen peroxide	Santoku Chemical Industry Co.	18412-15; CAS 7722-84-1
BOBO™-1 Iodide	Thermo Fisher Scientific	B3582
benzyl alcohol	TOKYO CHEMICAL INDUSTRY CO., LTD.	#B2378; CAS 100-51-6
benzyl benzoate	TOKYO CHEMICAL INDUSTRY CO., LTD.	#B0064; CAS 120-51-4
silicone oil	Shin-Etsu Chemical	HIVAC-F4; CAS 63148-58-3
mineral oil	Sigma-Aldrich	M8410; CAS 8042-47-5
Critical commercial assays		
DR-A1	ATAGO CO., LTD	NO1310
IVIS Lumina X5 Imaging System	Revvity	CLS148590
11.7 T MRI scanner	Bruker	AVANCE II 500WB
Experimental models: Cell lines		
G-292 clone A141B1	JCRB cell bank	IFO50107; RRID:CVCL_2909
Software and algorithms		
Ilastik	ilastik team	Version 1.4.0.post1; RRID:SCR_015246
3D Slicer	Slicer Community	5.8.1; RRID:SCR_005619
IMARIS	Oxford Instruments company	7.6.1; RRID:SCR_007370
Python	Python Software Foundation	3.6.4; RRID:SCR_008394

EXPERIMENTAL MODEL AND STUDY PARTICIPANT DETAILS

Animals

C57BL/6N mice (CLEA Japan, Inc.), 8 weeks of age, were utilized to create a whole-organ atlas at single-cell resolution. Both male and female mice were used for construction of the adult organ atlas. For sampling, the mice were deeply anesthetized using isoflurane. Subsequently, they were transcardially perfused with PBS (15mL) to remove blood from the organs, followed by perfusion with 4% PFA (15mL). The excised organs (thyroid, salivary gland, heart, lung, liver, pancreas, kidney, bladder, epididymis, testis and uterus) were fixed using PFA at 4°C for 48 hours. Male C57BL/6N mice (CLEA Japan, Inc.) at ages of 1 week, 2 weeks, 3 weeks, and 5 weeks were perfused, and the kidneys were excised and fixed with the same protocol.

To create a mouse model of cisplatin-induced acute renal failure, 8-week-old male C57BL/6N mice (CLEA Japan, Inc.) were administered a single intraperitoneal injection of cisplatin dissolved in saline (1 mg/ml, total dose of 20 mg/kg, Fujifilm, 033-20091).[90] Control of animals received an equivalent volume of saline. After 72 hours, the mice treated with cisplatin dissolved in saline (n = 3), and those treated with saline (n = 3) were perfused and the kidneys were excised.

To create a mouse model of LPS-induced acute lung injury, 8-week-old male C57BL/6N mice (CLEA Japan, Inc.) were anesthetized with a three-drug combination anesthesia consisting of medetomidine (0.3 mg/kg), midazolam (4 mg/kg), and butorphanol (5 mg/kg), and subsequently administered *Escherichia coli* LPS dissolved in PBS (5 mg/ml; total dose, 5 μg/g body weight; Sigma-Aldrich, L2880) intratracheally through a 22-gauge catheter.[91] Control of animals received an equivalent volume of PBS. 96 hours later, the mice treated with LPS dissolved in PBS (n = 3), and those treated with PBS (n = 3) were perfused and the lungs were excised.

To create a mouse model of osteosarcoma lung metastasis, SCID-beige mice (CB17.Cg-Prkdc^{scid}Lyst^{bg-J}/ CrlCrlj, Charles River Laboratories), 6 weeks of age, were intravenously injected with G-292 clone A141B1 (JCRB cell bank, IFO50107) cells stably expressing ZsGreen and Akaluc genes (G-292/ZsGreen-Akaluc, 5 × 10^5 cells/mouse)[69]. LPAR1 antagonist (ONO-7300243, 30 mg/kg, Cayman Chemical Company, 22052) or corn oil (Nacalai Tesque, 25606-65) as a vehicle was administered orally 60 minutes prior to tumor cell injection (n = 8 per group). 24 hours later, in vivo imaging was performed using the IVIS Lumina X5 Imaging System (Revvity, CLS148590), followed by perfusion fixation and lung excision.

To create an atlas of the whole body of neonatal mice, cesarean sections were performed on pregnant mice at 18.5 days of gestation. Subsequently, male and female neonatal mice were sacrificed by an overdose of isoflurane and then fixed in 4% paraformaldehyde (PFA) at 4°C for 96 hours. Both male and female neonatal mice were included.

All experimental procedures and housing conditions were approved by the committee of the RIKEN institute, and all animals were cared for and handled humanely in accordance with the institutional guidelines for animal experiments. Both sexes were included for adult atlas construction and neonatal whole-body analysis, whereas only male mice were used for the cisplatin and LPS models, the developmental kidney series, neonatal immunostaining experiments, and the osteosarcoma lung metastasis model; sex-specific effects were not formally tested for disease models and may limit generalizability. During atlas construction, sex-related differences in organ size and total cell numbers were noted. Mice were maintained under specific pathogen-free (SPF) conditions with a standard light/dark cycle and had ad libitum access to food and water.

Cell lines

The human osteosarcoma cell line G-292 (clone A141B1; JCRB Cell Bank, IFO50107) was used for the lung metastasis model. Cells were genetically modified to stably express ZsGreen and Akaluc (G-292/ZsGreen-Akaluc) as previously reported[69]. Cells were maintained according to the supplier's recommended conditions.

METHOD DETAILS

Tissue clearing and staining of adult mouse organs using the CUBIC protocol

All organs were subjected to delipidation with CUBIC-L, nuclear staining with Propidium iodide (PI), and RI matching with CUBIC-R+[50]. CUBIC-L consisted of 10 wt% N-butyldiethanolamine and 10 wt% Triton X-100 in distilled water, and CUBIC-R+ consisted of 45 wt% antipyrine, 30 wt% nicotinamide, and 0.1% (vol/vol) N-butyldiethanolamine in distilled water. The refractive index of CUBIC-R+ was adjusted to 1.522 using a digital refractometer (DR-A1; ATAGO CO., LTD). Both CUBIC-L and CUBIC-R+ are commercially available from CUBICStars Inc. Between each step, the organs were washed three times with PBS. Each step was carried out at 37°C, and the processing time was optimized for each organ (Figure S1A). Delipidation with CUBIC-L was performed using CUBIC-L diluted to 50% with distilled water for the first day. The volume of CUBIC-L was 10 ml for all organs except the liver, for which 20 ml was used. The amount of PI used for nuclear staining was as follows: 1.41 μg for the thyroid, 37.2 μg for the salivary glands, 33.9 μg for the heart, 67.9 μg for the lungs, 320 μg for the liver, 12.6 μg for the pancreas, 48.8 μg for the kidneys, 0.744 μg for the bladder, 5.13 μg for the epididymis, 17.4 μg for the testes, and 10 μg for the uterus, with a final concentration of 30 μg/ml. RI matching with CUBIC-R+ was performed using 50% diluted CUBIC-R+ for the first day for all organs except the liver. The liver was processed for RI matching with 20% CUBIC-R+ for 2 days, 40% CUBIC-R+ for 2 days, 60% CUBIC-R+ for 2 days, 80% CUBIC-R+ for 2 days, and 100% CUBIC-R+ for 3 days. The volume of CUBIC-R+ was 10 ml for all organs except the liver, for which 20 ml was used. For αSMA immunostaining of the lungs, the CUBIC-HV protocol was used[51]. Anti-αSMA antibody (2.0 μg,

Sigma-Aldrich, A5228) was applied in 500 μl of immunostaining buffer, and the samples were shaken at 37°C for 7 days. The immunostaining buffer was HEPES-TSC buffer [10 mM HEPES (pH 7.5), containing 0.1% (v/v) Triton X-100, 200 mM NaCl, and 0.5% (w/v) casein]. The secondary antibody used was Alexa594-labeled Anti-Mouse IgG2a antibody (1.3 μg, Jackson Immuno Research, 115-587-186). CUBIC-HV staining reagents are also commercially available from CUBICStars Inc.

Tissue Clearing, Nuclear Staining, and Immunostaining of Neonatal Mice

Neonatal mice were processed with CUBIC-L for delipidation, hydrogen peroxide for depigmentation, CUBIC-B for decalcification, PI for nuclear staining or immunostaining, and CUBIC-R+ for RI matching. Delipidation with CUBIC-L was performed at 37°C for 10 days using 10 ml per sample, with the first 2 days using CUBIC-L diluted to 50% with water. Depigmentation with hydrogen peroxide (3%, 10 ml/sample, Santoku Chemical Industry Co., 18412-15) was carried out at 25°C for 4 days using 10 ml per sample. Decalcification with CUBIC-B was conducted at 37°C for 4 days using 10 ml per sample. Nuclear staining with PI was performed at 37°C for 5 days using 700 μg per sample at a concentration of 175 μg/ml. For samples intended for immunostaining, BOBO™-1 Iodide (8 μl/sample, Thermo Fisher Scientific, B3582) was used for nuclear staining. Immunostaining was performed following the CUBIC-HV protocol[50]. A staining buffer volume of 1.2 ml was used, and for IBA1 immunostaining, Anti-IBA1 antibody (10 μg, Abcam, ab178847) was used; for TH immunostaining, Anti-Tyrosine Hydroxylase antibody (18 μg, Abcam, ab137869) was used; and for αSMA immunostaining, Anti-αSMA antibody (7.5 μg, Sigma-Aldrich, A5228) was used, with all samples shaken at 25°C for 30 days. Alexa594-labeled Fab antibodies were used as secondary antibodies. For IBA1 immunostaining, the secondary antibody was anti-Rabbit IgG (6.7 μg, Jackson Immuno Research, 111-587-008), and the same secondary antibody was used for TH immunostaining (12 μg, Jackson Immuno Research, 111-587-008). For αSMA immunostaining, the secondary antibody was Anti-Mouse IgG2a (5.0 μg, Jackson Immuno Research, 115-587-186). RI matching with CUBIC-R+ was carried out at 37°C for 5 days using 10 ml per sample, with the first day using CUBIC-R+ diluted to 50% with water.

Tissue Clearing of Adult Mouse Organs Using the BABB Protocol

Hearts, lungs, and kidneys from 8-week-old mice were first processed with CUBIC-L for delipidation and stained with PI as described above. After nuclear staining, the samples were washed three times with PBS (10mL) for 30 min each. The organs were then dehydrated in a graded methanol series at 25°C with gentle shaking: 60% (vol/vol) methanol in water for 4 h, 80% (vol/vol) methanol in water (10mL) for 4 h, and 100% methanol (10mL) overnight, followed by an additional incubation in fresh 100% methanol (10mL) for 4 h. Finally, the organs were immersed in BABB solution (10mL, benzyl alcohol (TCI, #B2378) and benzyl benzoate (TCI, #B0064) mixed at a 1:2 volume ratio) until they became optically transparent.[27]

Volume Correction using MRI data

To correct for tissue expansion caused by CUBIC processing, MRI imaging was performed. Magnetic resonance imaging (MRI) was performed using an 11.7 T MRI scanner (AVANCE II 500WB, Bruker BioSpin, Ettlingen, Germany) equipped with gradient coils providing a maximum gradient strength of 1.5T/m and a slew rate of 10000T/m/s. Mice were euthanized by carbon dioxide (CO_2) inhalation immediately prior to imaging. T1-weighted multi-slice images were acquired using a fast low-angle shot (FLASH) sequence with the following parameters: repetition time (TR) of 100 ms, echo time (TE) of 2.15 ms, field of view (FOV) of 25.00 mm × 25.00 mm, acquisition matrix of 256 × 256 (resulting in an in-plane resolution of 97.66 μm × 97.66 μm per pixel), slice thickness of 0.1 mm, and 200 slices. The acquired MRI datasets were segmented for the salivary gland, heart, lung, liver, pancreas, kidney, bladder, epididymis, and testis using 3D Slicer software by a clinical pathologist. Organ volumes were calculated from the segmented images by multiplying the total number of voxels within each segmented organ by the voxel volume determined from the image resolution. For each organ, cell density measurements obtained from CUBIC-processed tissues were corrected by the ratio of the MRI-derived volume to the post-clearing volume of the same organ. This correction was applied uniformly across all samples to account for tissue size changes introduced during the clearing process and was performed prior to statistical comparisons.

Construction of a Customized Light-Sheet Microscope

The customized light-sheet fluorescence microscope used in this study, designated exMOVIE, was developed based on our previously reported MOVIE system[39] and incorporates several critical modifications to enable high-resolution imaging of large and cleared tissue samples. This system is not commercially available but is fully open source in terms of hardware and software specifications to promote reproducibility and adoption by other laboratories.

The microscope employs three continuous-wave lasers: 488 nm (Cobolt, 06-MLD, 200 mW), 532 nm (MPB Communications, 500 mW), and 647 nm (Cobolt, 06-MLD, 130 mW). The laser beams are coupled into the illumination path through a dichroic mirror system, replacing the mSPIM galvano mirror of the original MOVIE system to enable Axially Swept Light Sheet Microscopy (ASLM). The light sheet focus is dynamically adjusted using an electrically tunable lens (ETL), which is synchronized with the rolling shutter readout of a scientific CMOS camera (Hamamatsu, ORCA-Flash4.0 V3) to maintain axial resolution across the entire field of view.

The sample chamber was custom-fabricated using transparent acrylic with mounted slide-glass windows and filled with a silicone oil–mineral oil mixture adjusted to a refractive index of 1.522 to match the CUBIC-R+ clearing solution, thereby minimizing refractive index mismatches. Samples were mounted on a high-precision motorized stage composed of an XZ translational stage (Surugaseiki,

KY1250), a Y translational stage (Kohzuseiki, ZA16A-X101), and a theta rotation stage (Sigmakoki, OSMS-60YAW). This configuration enabled imaging of whole organs from both front and back with subcellular spatial fidelity.

All hardware components—including lasers, camera, ETL, and motorized stages—were coordinated using a custom-developed control software written in Visual Studio (C++/CLI). This software regulates synchronization for ASLM imaging and provides user interface control for three-dimensional scanning.

To ensure reproducibility, we have made the complete parts list, including objective lens specifications (Table S3), CAD drawings of the microscope components, and the full control software freely available to the research community via Zenodo under a permanent DOI (https://doi.org/10.5281/ZENODO.18028197).[89] The corresponding GitHub repository is available at https://github.com/OrganismalSystemsBiology/WholeOrganAtlas. The objective lens used in this system is a 10×, NA 0.6 long-working-distance lens (Olympus, XLPLN10XSVMP), which supports high numerical aperture imaging in high-RI media. These open resources are intended to facilitate adoption and adaptation of the exMOVIE system by other groups, including those seeking to generate compatible data with our CUBIC-based Organ Atlas. A detailed comparison of the imaging systems with commercially available light-sheet microscopes, including objective specifications, scanning speed, clearing compatibility, and resolution, is provided in Table S4.

For obtaining lower resolution images in Figures 5, 7, and S1, we also built a low-magnification light sheet microscope, which was utilized for rapidly acquiring 3D images of entire organs.[92] The MOVIE-scan method was implemented for rapid imaging. In low-magnification imaging, when using a low NA objective lens with a long focal depth, the MOVIE-focus method is not required. The lasers used were 488 nm (Cobolt, 04-series, 200 mW), 532 nm (Cobolt, 06-series, 300 mW),592 nm (MPB, 300 mW), and 647 nm (MPB, 300 mW). To improve z-resolution, this LSFM did not use the ASLM system, instead using the column tiling method. Approximately 18 tiles are captured for a mouse brain. The parts list and CAD data for this microscope are available from the original publication.[91]

Three-Dimensional Imaging of Whole Organs and the Entire Body at Cellular Resolution

Organs and whole-body samples that were subjected to RI matching were embedded in an agarose gel mixed with CUBIC-R+ and then imaged while being immersed in a mixture of silicone oil HIVAC-F4 (Shin-Etsu Chemical) and mineral oil (M8410, Sigma-Aldrich), with the refractive index adjusted to 1.522 to match that of CUBIC-R+.[39] The light sheet microscope used for imaging was equipped with a 10x objective lens with a sensor size of 13.3 mm, providing a field of view of 1.33 mm. Since this field of view was insufficient to cover the entire sample, tiling was employed to obtain whole-organ or whole-body images. The tiling procedure followed previously reported methods, with adjacent tiles overlapping by 100 to 124 pixels in the XY direction. To enable imaging of samples to be thicker than the working distance of the lens and to obtain high-quality images even for small samples, imaging was conducted from both the front and back surfaces of the sample. The sample was rotated along the Y-axis and imaged at $\theta = 0^\circ$ and $\theta = 180^\circ$, thereby capturing images from the opposite side as well. The rotation center was determined by manually aligning identical cells or structures. Additionally, an overlap of 100 μm to 400 μm was ensured along the Z-axis, and the Z-start position was set to acquire stack images at 2.5 μm steps. Imaging was performed using the MOVIE system with ASLM, with an exposure time of 30 ms and an imaging speed of 33 fps with 500 mW. Each image was approximately 8.4 MB (2,048 × 2,048 pixels, 16-bit), resulting in a data acquisition rate of 270 MB/second. For example, imaging the entire neonatal mouse yielded approximately 2.4 million images, totaling 20 TB of data, which was completed within 72 hours, including stage movement time. The acquired data was directly transferred to server storage via a 56 Gbps InfiniBand system.

Three-Dimensional Imaging of Lungs with Metastasized Tumor Cells Expressing ZsGreen and Whole-Body Immunostained Neonatal Mice

A custom-made low-magnification (1x) light sheet microscope was used for imaging the lungs with metastasized tumor cells expressing ZsGreen and for whole-body imaging of immunostained neonatal mice. For imaging the lungs, a 488 nm laser was used to capture ZsGreen with an exposure time of 150 ms with 200 mW. For whole-body imaging of neonatal mice, nuclear staining with BOBO-1 was captured using a 488 nm laser with an exposure time of 50 ms. Additionally, IBA1, TH, and αSMA, all labeled with Alexa594, were captured using a 592 nm laser with an exposure time of 50 ms with 500 mW.

Experimental design and reporting considerations

All experiments were performed using biologically independent animals, and exact sample sizes (n) are reported in the corresponding figure legends. Animals were assigned to treatment or control groups prior to dosing in the cisplatin-induced acute kidney injury, LPS-induced acute lung injury, and osteosarcoma lung metastasis experiments. Blinding was not applied during image acquisition or computational analysis due to the nature of large-scale automated imaging; manual segmentation and anatomical annotation were performed by trained investigators, including a clinical pathologist. Sample sizes were determined based on prior experience with similar whole-organ imaging studies and feasibility constraints. Animals with technical failure during perfusion or severe tissue damage were excluded prior to imaging, and no data points were excluded after quantitative analysis.

QUANTIFICATION AND STATISTICAL ANALYSIS

Nuclear Detection

For nucleus detection, we used the previously reported HDoG filter based method.[39] The kernel size of the larger Gaussian filter of the HDoG filter was set to 1.5 times that of the smaller Gaussian filter. The kernel size of the smaller Gaussian filter was set to 4.5 voxels for the heart and epididymis and to 4 voxels for other organs and whole-body samples. The HDoG filter was applied to compute the Hessian matrix and to identify candidate regions for cell nuclei by selecting voxels showing three negative eigenvalues of the Hessian matrix. Next, three features were calculated: the maximum intensity within each region, the structureness of the region defined as a measure calculated from the square root of the sum of the squared eigenvalues of the Hessian matrix, and the difference between the average intensity within the region and the average intensity within a 10-pixel surrounding area. These features were used to determine whether the candidate regions were actual cell nuclei, followed by segmentation of the nuclei, with parameter tuning performed by visual inspection of candidate maps for each organ.[39] The centroid of each segmented region was considered the position of the cell. To evaluate detection accuracy, ground truth annotations were manually created by experienced annotators on randomly selected regions. Specifically, two independent experts including one clinical pathologist manually labeled nuclear centroids in selected 3D image stacks. True positives, false positives, and false negatives were calculated by comparing detected coordinates to the ground truth (Figure S2).

Detection of IBA1-Positive Cells

The detection of IBA1-positive cells of neonatal mice was performed using the previously reported ilastik workflow.[43] The signals were classified into three categories: positive cell signals, bright but non-positive cell signals, and background. The image feature descriptors selected were Gaussian (σ = 0.3, 0.7 voxels), Gaussian gradient magnitude (σ = 0.7 voxels), difference of Gaussians (σ = 0.7, 1.0, 1.6, 3.5 voxels), and Hessian of the Gaussian eigenvalues (σ = 1.0, 1.6, 3.5 voxels). Tiff images were manually annotated in sets of 150 using ilastik software. The trained voxel classifier was then applied to each image in batch processing to generate probability maps for IBA1-positive cells throughout the body. By detecting positive cells from the probability maps using a threshold of 0.7, IBA1-positive cells were identified across the entire body.

Stitching and alignment of large organ-wide 3D image stacks

In high-magnification light sheet microscopy, whole-organ imaging was performed by dividing the sample into overlapping tiles (stacks) from both the front and reverse sides, with an overlap of 100 to 124 pixels in the x–y direction (Figure S3A). Due to mechanical deviations (e.g., pitching and yawing), simple alignment based on stage movement was insufficient, necessitating an image-based stitching approach (Figure S3B).

First, visible sample regions were automatically detected in each stack. For each overlapping region, we used the OpenCV template matching library with Normalized Cross-Correlation (NCC) to compute brightness-based similarity. NCC was calculated across 100 z-slices, and the best-matching plane was selected to determine 3D displacement between adjacent stacks (Figures S3D–S3F). These displacement vectors were used to stitch stacks within each side (FW and RV) (Figure S3C, Step 1).

Next, the FW and RV datasets were aligned. Central stacks from both sides were initially registered using the ANTs rigid registration algorithm to estimate skew angles and translational offsets (Figure S3C, Step 2). Angle and displacement were calculated across 9 to 25 tiles, and the tile pair with minimal registration error was used to define the rotation matrix (Figure S3C, Step 3). This matrix was then used to rotate all RV stacks globally. The rotated RV stacks were stitched to the FW stacks using NCC-based alignment (Figure S3C, Step 4). Final global stitching parameters were obtained by linearly integrating these inter-side transformations with the intra-FW stitching data (Figure S3C, Step 5).

The quality of the stitching process was validated by reconstructing full 3D images, such as those of the liver (Figures S3G and S3H). After image stitching, the same transformation matrices were applied to the detected nuclear coordinates to produce a fully aligned and spatially accurate cell coordinate map. Cell detection was performed on the entire acquired image, and for overlapping regions between tiles, we removed the redundant portions based on the stitching parameters to prevent duplicate detections. This approach ensured accurate 3D nuclear position information without redundancy in the overlapping regions.

Calculation of Organ Volume and Cell Density in Mice

To determine the organ volumes, the coordinates of the nuclei, corrected by stitching, were used to create nuclear density images using the histogramdd method in NumPy library. For the thyroid and bladder, nuclear density images were generated with a voxel size of 10 μm, while for other organs, a voxel size of 50 μm was used. In the case of the thyroid, since tissues other than the organ itself were also captured in the images, the thyroid region was segmented using the 3D Slicer[56], and a nuclear density image specific to the thyroid was generated. Using these nuclear density images, the number of voxels containing cells was determined. The organ volumes were then calculated by counting the number of voxels containing cells. Finally, the average cell density of each organ was obtained by dividing the total number of cells in each organ by the calculated organ volume.

Segmentation and Creation of the CUBIC Organ/Body Atlas

Anatomical region segmentations for the heart, lung, liver, kidney, and neonatal body were generated from nuclear density images. For adult organs, density images were computed at a voxel size of 50 μm, whereas neonatal body segmentation used 100 μm voxels. For validation of bronchial and arterial segmentation in the lung, α-smooth muscle actin (αSMA) immunostaining images (50 μm voxels) were additionally acquired.

All segmentations were performed in 3D Slicer[56]. First, organ volume images were converted into binary masks using global thresholding. Anatomical regions were manually delineated by a histopathology expert based on nuclear-density differences and known macroscopic landmarks. Segmentation refinement was achieved using the Grow from Seeds module, enabling the propagation of initial labels throughout the volume. To generate anatomically smooth boundaries, label maps were further processed using morphological smoothing following established procedures.[57]

For each organ, the anatomical label of each nucleus was determined by mapping its coordinates onto the segmentation volume, thereby assigning region identity to every detected cell. This procedure produced the region-annotated CUBIC Organ/Body Atlas for male and female organs.

Mapping and Annotation to the CUBIC Organ/Body Atlas

For image registration, nuclear density images or nuclear-stained images were used as sample images, while nuclear density images from the CUBIC Organ/Body Atlas were used as reference images. Images with a voxel size of 50 μm were used for organ registration, and images with a voxel size of 100 μm were used for whole-body registration. The registration calculations for organs and whole-body were performed using affine transformation and the symmetric diffeomorphic image registration (SyN) algorithm from the ANTs library, as previously reported for brain registration[39]. For the kidneys and the hearts, whole-organ registration was performed, while for the lungs and liver, segmentation and registration were conducted for each lobe individually. In the registration of neonatal mice, nuclear density images were used for experiments where all cells were detected, and nuclear-stained images were used for experiments involving IBA1 immunostaining. Additionally, due to the high degree of freedom in the skin of neonatal mice, an erosion filter with a kernel size of $5\times5\times5$ was applied to remove the skin from the images before registration. The transformations calculated from each registration were applied to the coordinates of the detected positive cells and then mapped to the nearest-neighbor cells in the CUBIC Organ/Body Atlas using the scipy.spatial.cKDTree implementation from the SciPy library. Annotation information was obtained by referencing the anatomical regions associated with the nearest-neighbor cells in the CUBIC Organ/Body Atlas. In cases where some parts, such as the limbs, could not be registered in neonatal mice, these regions were segmented and manually annotated using 3D Slicer.

Whole-kidney cell-profiling of mice at different ages

All cells in the kidneys of 1-week-old, 2-week-old, 3-week-old, and 5-week-old mice were detected and mapped to the CUBIC Organ Atlas. Using the annotation information obtained from the mapping, the number of cells, the volume of the region, and the cell density in each region at each time point were calculated. The cell density was corrected using the volume determined by in vivo MRI imaging. The medulla was divided into 10 layers based on distance, and the cell number in each layer was normalized by the average cell number for each week. For clustering the 10 layers using these normalized cell numbers, Ward's method based on Euclidean distance from the SciPy library was used.

Statistical Analysis

We employed a negative binomial regression model using Python's statsmodels library (version 0.12.2) to compare cell counts, which throughout this study refers to the number of detected cells in each analyzed organ and glomeruli counts between groups. The significance of the differences between groups was assessed using False Discovery Rate (FDR) correction, with p-values less than 0.05 considered statistically significant. Results with p-values equal to or greater than 0.05 were considered not significant (n.s.). For density and volume comparisons, Student's t-test was performed using Scipy library (version 1.5.4). In the analysis of in vivo imaging in the lungs, the Mann-Whitney U test was used, with significance set at $^*p<0.05$, and results with p-values equal to or greater than 0.05 were considered not significant (n.s.). n denotes biologically independent animals unless otherwise stated in figure legends, and data are reported as mean ± SD unless otherwise specified. The source data used for the statistical analyses are provided as Excel files and are available at https://whole.cfosdb.systems-based-medicine.org/whole_body/resource.

Computational Requirements for Atlas Processing

To address scalability considerations for processing and analyzing large-scale whole-organ and whole-body datasets, we summarized the hardware specifications required for each major analysis step in our pipeline (Table S5). These specifications were determined based on the computational infrastructure used in this study. For stitching, more than 20 CPU cores and 128 GB of system memory were required. Segmentation could be performed with a single CPU core and 32 GB of memory. Point detection was GPU-accelerated, requiring more than four CPU cores, over 11 GB of GPU memory, and 16 GB of system memory. Registration requires more than 20 CPU cores and 16 GB of system memory, while point transfer could be completed with a single CPU core and 16 GB of system memory.

The microscope control software, registration programs, and 3D stitching codes used in this study are available via Zenodo under a permanent DOI (https://doi.org/10.5281/ZENODO.18028197)[89]. The corresponding GitHub repository is available at https://github.com/OrganismalSystemsBiology/WholeOrganAtlas.

ADDITIONAL RESOURCES

Generated data, including atlas datasets, are available at https://whole.cfosdb.systems-based-medicine.org/whole_body/.

Supplemental figures

A

	Fixation	Delipidation	Staining	RI matching
Thyroid	2 days	5 days	5 days	5 days
Salivary gland	2 days	5 days	5 days	5 days
Heart	2 days	7 days	5 days	5 days
Lung	2 days	5 days	5 days	5 days
Liver	2 days	7 days	5 days	11 days
Pancreas	2 days	5 days	5days	5 days
Kidney	2 days	11 days	5 days	5 days
Bladder	2 days	5 days	5 days	5 days
Epididymis	2 days	5 days	5 days	5 days
Testis	2 days	5 days	5 days	5 days
Uterus	2 days	5 days	5 days	5 days

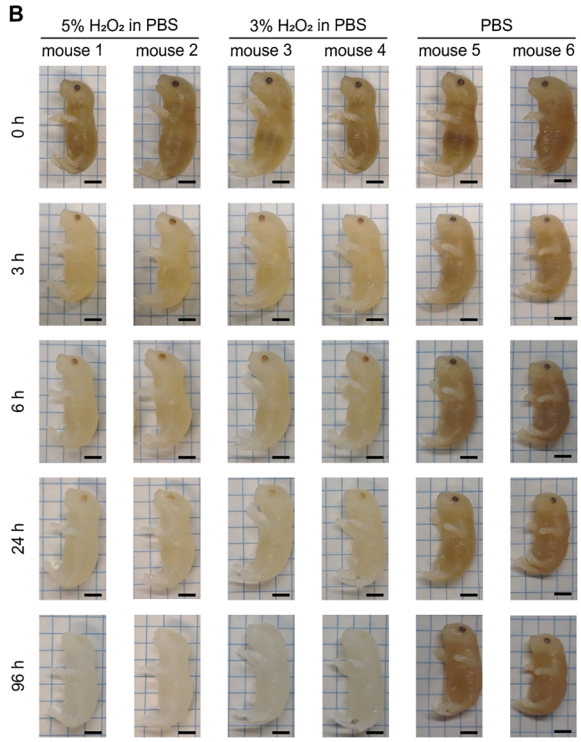

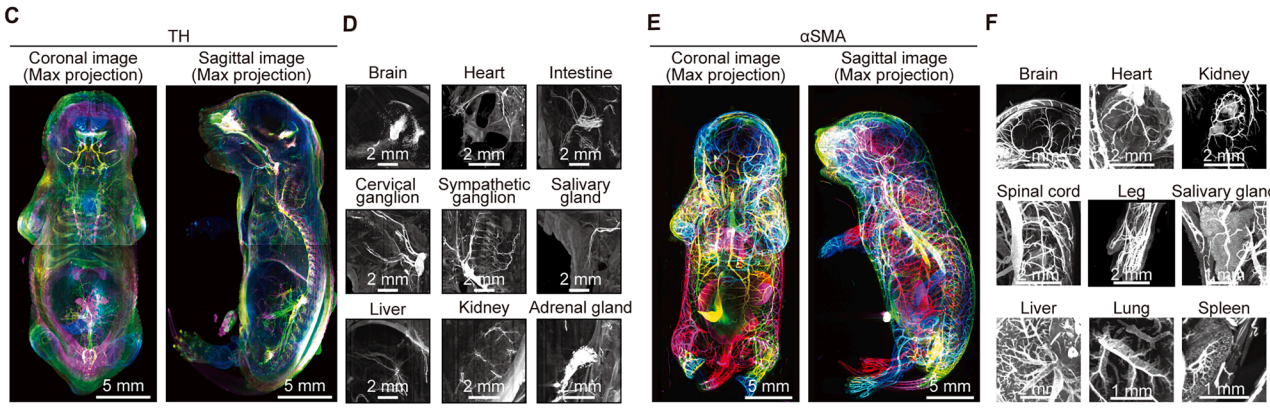

Figure S1. Optimized tissue clearing procedures and whole-body 3D immunostaining, related to Figure 1

(A) Summary of the optimized tissue clearing protocol for multiple mouse organs. The table lists the duration of each step—fixation, delipidation, staining, and refractive index (RI) matching—for the thyroid, salivary gland, heart, lung, liver, pancreas, kidney, bladder, epididymis, testis, and uterus.

(B) Depigmentation of newborn mice treated with 5% H_2O_2 in PBS, 3% H_2O_2 in PBS, or PBS alone. Representative images at 0, 3, 6, 24, and 96 h show that 5% H_2O_2 in PBS caused strong depigmentation but introduced bubble formation, whereas 3% H_2O_2 in PBS achieved effective depigmentation, including in the eyes, without damaging tissues. PBS alone showed no appreciable depigmentation. Scale bars, 5 mm.

(C and D) 3D whole-body immunostaining of TH.

(C) Maximum intensity projection images (coronal and sagittal), with depth color-coded every 1,500 μm (red, magenta, green, yellow, cyan, blue).

(D) Enlarged projection images of selected anatomical regions showing TH signals.

(E and F) 3D whole-body immunostaining of α-SMA (α-smooth muscle actin).

(E) Maximum intensity projection images (coronal and sagittal), with depth color-coded every 1,500 μm (red, magenta, green, yellow, cyan, blue).

(F) Enlarged projection images of selected anatomical regions showing α-SMA signals.

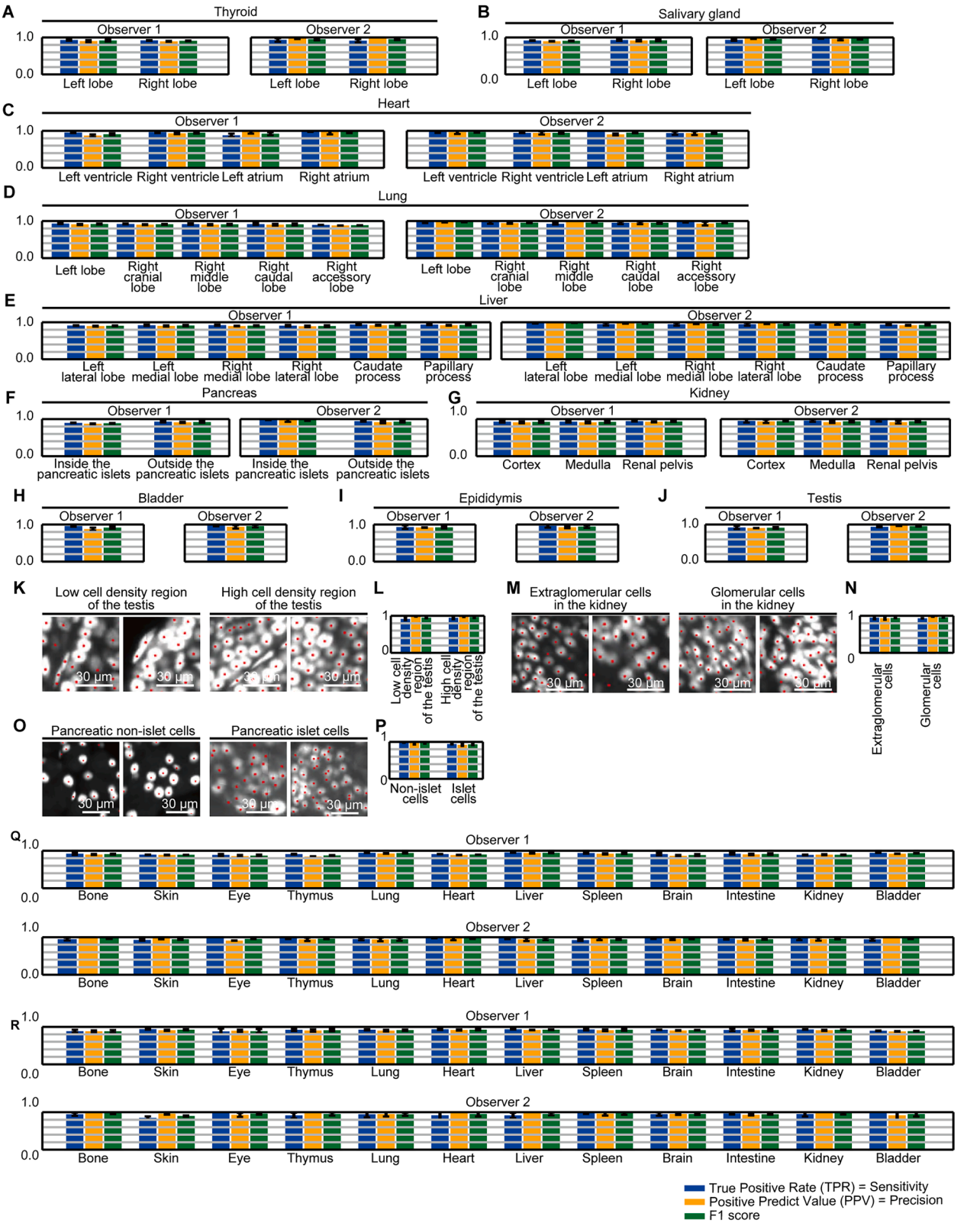

(legend on next page)

Figure S2. Accuracy of cell detection across different organs and regions, related to Figures 2, 6, and 7

(A–J) Bar plots showing the performance of the cell detection algorithm in terms of the TPR (TPR = sensitivity), PPV (PPV = precision), and F1-score across multiple organs and regions. Data are shown for two independent observers, each of whom evaluated three randomly chosen sites per region.

(A) Thyroid (left and right lobes).

(B) Salivary gland (left and right lobes).

(C) Heart (left ventricle, right ventricle, left atrium, right atrium).

(D) Lung (left lobe, right cranial lobe, right middle lobe, right caudal lobe, accessory lobe).

(E) Liver (left lateral lobe, left medial lobe, right medial lobe, right lateral lobe, caudate process, papillary process).

(F) Pancreas (inside and outside the pancreatic islets).

(G) Kidney (cortex, medulla, renal pelvis).

(H) Bladder.

(I) Epididymis.

(J) Testis.

(K–P) Evaluation of detection accuracy in high-cell-density regions.

(K and L) Representative images of low- and high-cell-density regions in the testis; red dots indicate detected nuclei. Quantitative assessment is shown in (L).

(M and N) Representative images of extraglomerular and glomerular regions in the kidney with detected nuclei. Quantitative evaluation is shown in (N).

(O and P) (O) Representative images of pancreatic non-islet and islet regions with detected nuclei, with corresponding accuracy metrics shown in (P).

Across these tissues, detection accuracy was slightly reduced in high-density areas (e.g., pancreatic islets, kidney glomeruli, high-density testis regions) but remained high overall.

(Q and R) Accuracy of cell detection in the whole-body dataset from neonatal mice.

(Q) TPR, PPV, and F1-score for nuclear detection across bone, skin, eye, thymus, lung, heart, liver, spleen, brain, intestine, kidney, and bladder. TPR ranged from 89% to 100% and PPV from 84% to 100%. (R) Detection accuracy for IBA1-positive cells across the same organs, with TPR of 88%–94% and PPV of 88%–92%.

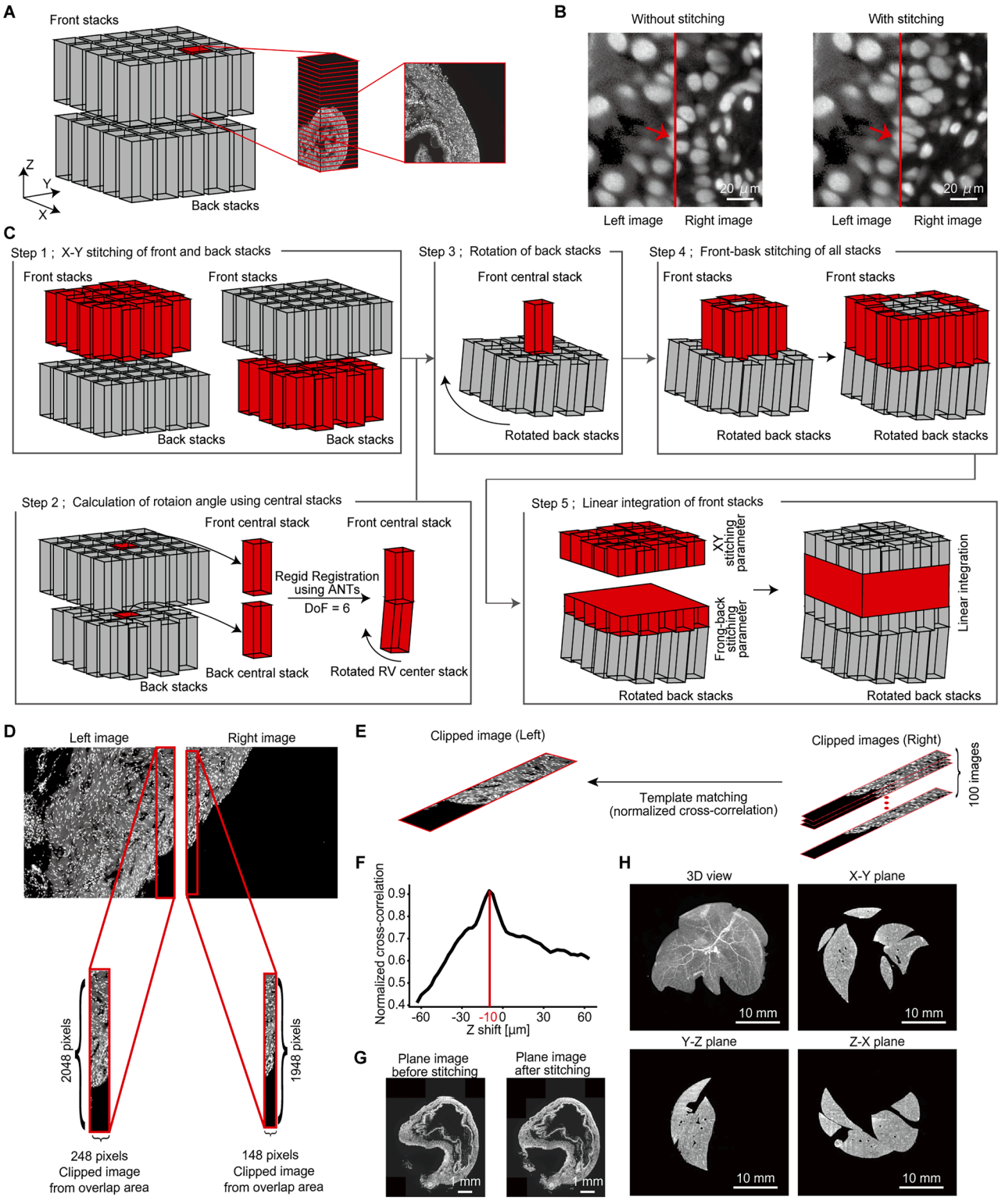

Figure S3. Optimized workflow for stitching large-scale 3D organ-wide image data, related to Figures 2 and 6

(A) Schematic showing the front and back stacks captured from two orthogonal sides, with an overlap of 100 pixels between neighboring stacks.

(B) Comparison of images before and after stitching, demonstrating the necessity of the stitching process to correct misalignments.

(legend continued on next page)

(C) Step-by-step workflow for stitching front and back stacks. Step 1: X-Y stitching of front and back stacks separately. Step 2: calculation of the rotation angle using the central stacks. Step 3: rotation of back stacks. Step 4: front-back stitching of all stacks. Step 5: linear integration of stitching parameters to calculate final stitching matrices.
(D) Comparison of the overlapping images. Magnified views showing the overlap areas used for cross-correlation calculations to align stacks.
(E) Illustration of the template matching process, showing the correlation calculation across 100 consecutive Z plane images to determine the optimal Z shift for 3D stitching.
(F) Graph showing the normalized cross-correlation curve, with the peak indicating the best alignment for Z shift during 3D stitching.
(G) Comparison of plane images before and after stitching, showing improved alignment in the stitched image.
(H) Final stitched 3D views of the liver in X-Y, Y-Z, and Z-X planes.

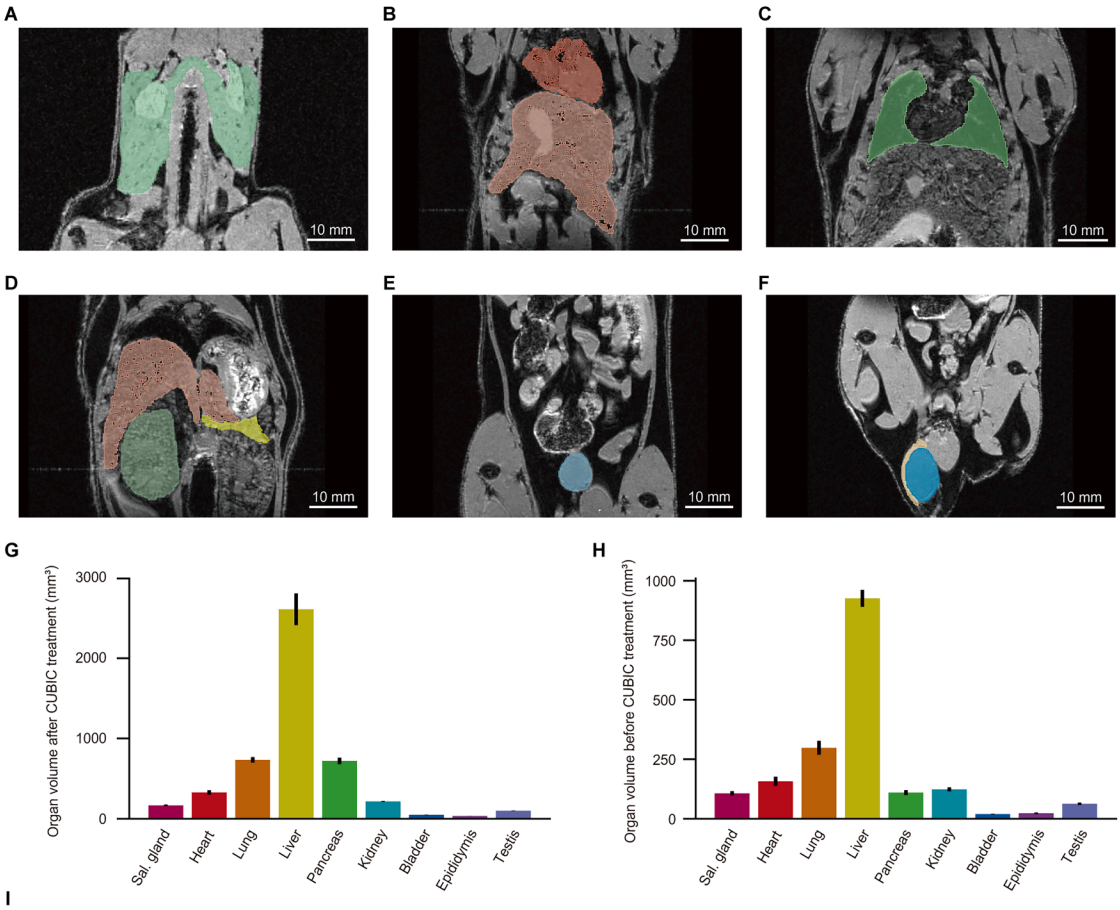

I

Organs	Cell number (cells, mean ± SD)	Cell density (cells/mm³, mean ± SD)
Thyroid	1.02×10^6 ($\pm 1.42 \times 10^4$)	2.64×10^5 ($\pm 7.18 \times 10^3$)
Salivary gland	4.32×10^7 ($\pm 2.23 \times 10^6$)	4.07×10^5 ($\pm 9.94 \times 10^3$)
Heart	2.81×10^7 ($\pm 1.07 \times 10^6$)	1.83×10^5 ($\pm 1.79 \times 10^4$)
Lung	1.20×10^8 ($\pm 5.20 \times 10^6$)	4.03×10^5 ($\pm 3.60 \times 10^3$)
Liver	2.94×10^8 ($\pm 1.64 \times 10^6$)	3.22×10^5 ($\pm 2.24 \times 10^4$)
Pancreas	7.52×10^7 ($\pm 4.17 \times 10^6$)	6.85×10^5 ($\pm 1.43 \times 10^4$)
Kidney	7.17×10^7 ($\pm 7.08 \times 10^5$)	5.83×10^5 ($\pm 1.16 \times 10^4$)
Bladder	5.10×10^6 ($\pm 8.81 \times 10^4$)	2.71×10^5 ($\pm 1.49 \times 10^4$)
Epididymis	1.20×10^7 ($\pm 6.33 \times 10^5$)	5.28×10^5 ($\pm 1.62 \times 10^4$)
Testis	5.14×10^7 ($\pm 1.31 \times 10^6$)	8.21×10^5 ($\pm 2.75 \times 10^4$)

Figure S4. Organ volume measurement using MRI and whole-organ cell numbers and cell densities, related to Figure 2

(A–F) Examples of organ segmentation in MRI images.
(A) Liver (green).
(B) Heart (red) and liver (ochre).
(C) Lung (green).
(D) Pancreas (yellow), kidney (green), and liver (ochre).
(E) Bladder (blue).
(F) Testis (blue) and epididymis (yellow).
(G) Organ volumes after CUBIC processing.
(H) Organ volumes before CUBIC processing measured by MRI.
(I) Whole-organ cell numbers and cell densities.
Table summarizing mean ± SD cell numbers and MRI-corrected cell densities across ten organs from 8-week-old C57BL/6N mice (thyroid density value is not MRI-corrected.)

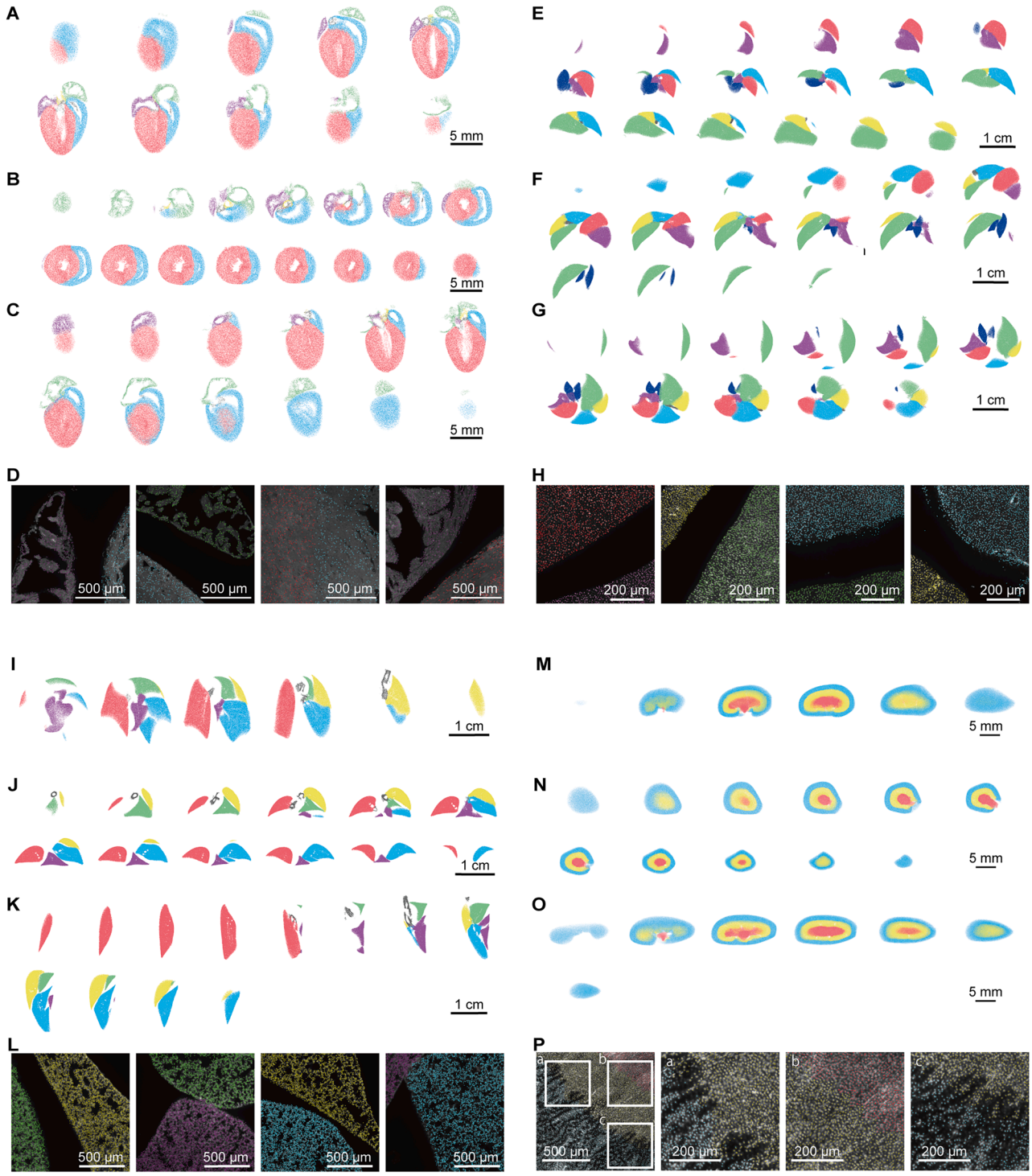

Figure S5. Single-plane images from single-cell-resolution organ atlases, related to Figure 3

(A–C) Whole heart atlas. Single-plane images from the single-cell-resolution mouse heart atlas shown in horizontal (A), sagittal (B), and coronal (C) views. Red represents the left ventricle, light blue the right ventricle, purple the left atrium, and yellow-green the right atrium. Slices are displayed at 0.80-mm intervals for all views.

(D) Heart raw image with annotations. Raw heart image overlaid with color-coded point annotations marking detected cells, with each color corresponding to its respective anatomical region.

(legend continued on next page)

(E–G) Whole lung atlas. Single-plane images from the single-cell-resolution mouse lung atlas representing horizontal (E), sagittal (F), and coronal (G) views. Red represents the left lobe, yellow-green the right cranial lobe, yellow the right middle lobe, light blue the right caudal lobe, and purple the right accessory lobe. Slices are displayed at 0.80-mm intervals for all views.
(H) Lung raw image with annotations. Raw lung image overlaid with color-coded point annotations marking detected cells for each anatomical region.
(I–K) Whole liver atlas. Single-plane images from the single-cell-resolution mouse liver atlas in horizontal (I), sagittal (J), and coronal (K) views. Yellow-green represents the left medial lobe, yellow the left lateral lobe, light blue the right medial lobe, red the right lateral lobe, purple the caudate process, and blue the papillary process. Slices are displayed at 1.5-mm intervals for all views.
(L) Liver raw image with annotations. Raw liver image overlaid with color-coded point annotations marking detected cells for each anatomical region.
(M–O) Whole kidney atlas. Single-plane images from the single-cell-resolution mouse kidney atlas representing horizontal (M), sagittal (N), and coronal (O) views. Light blue indicates the cortex, yellow the tubular system, and red the renal pelvis. Slices are displayed at 1.0-mm intervals for all views.
(P) Kidney raw image with annotations. Raw kidney image overlaid with color-coded point annotations marking detected cells in each anatomical region.

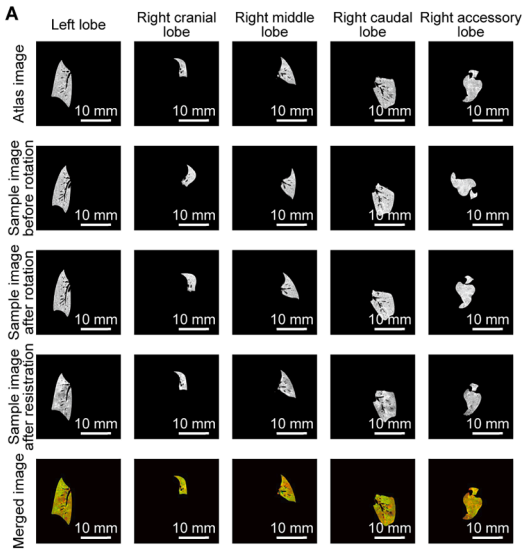

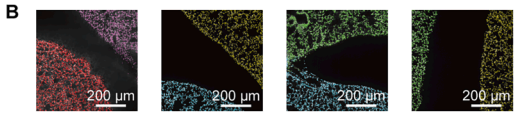

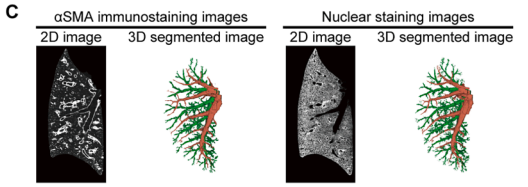

D

Accuracy	Trachea and bronchi	Artery
True Positive Rate	0.88	0.91
Positive Predict Value	0.92	0.92
F1 score	0.90	0.92

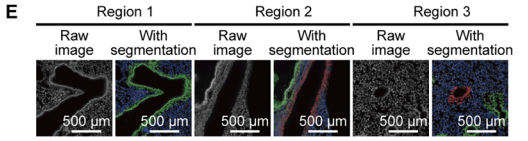

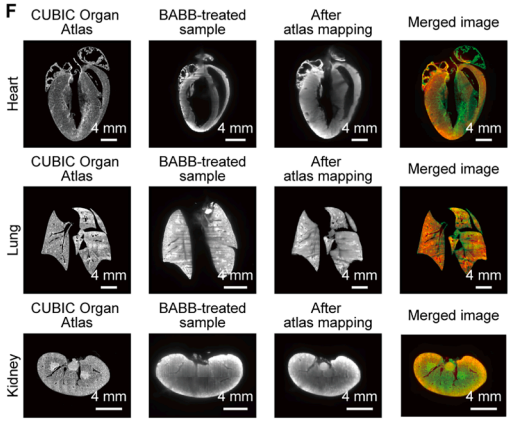

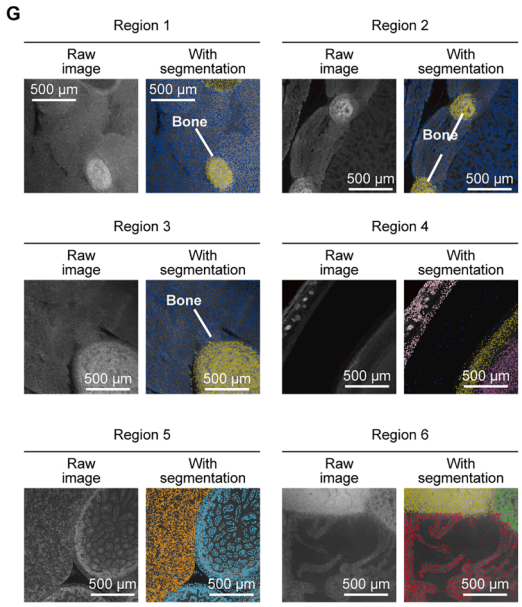

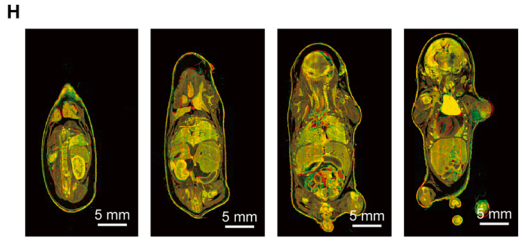

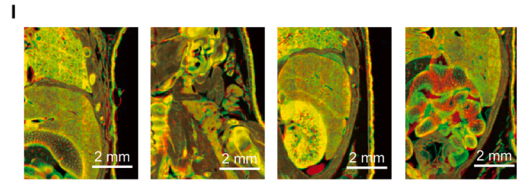

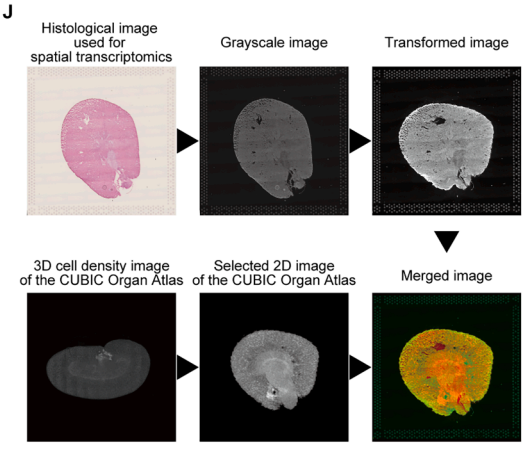

(legend on next page)

Figure S6. Validation of registration, segmentation accuracy, BABB compatibility, and registration of a spatial transcriptomics image, related to Figures 3, 6, and 7

(A) Step-by-step process for registering lung lobes by separating them into individual segments. Shown are reference atlas images of the five lung lobes (left, right cranial, right middle, right caudal, and right accessory); sample images before rotation, after rotation, and after lobe-wise registration; and merged images visualizing alignment of the atlas (green) and sample (red).

(B) Raw lung images overlaid with color-coded point annotations marking detected nuclei. Colors correspond to anatomical regions defined in the CUBIC Organ Atlas.

(C) Representative 2D and 3D segmented lung images derived from α-SMA immunostaining, with SMAs of bronchi (green) and arteries (red) specifically labeled (left). Corresponding 2D and 3D segmented images generated from nuclear-staining-based segmentation of the same regions are shown (right).

(D) Quantitative evaluation of segmentation accuracy using α-SMA-based masks as ground truth. Metrics include TPR, PPV, and F1 score for trachea/bronchi and arteries.

(E) Enlarged views of representative regions showing raw nuclear-staining images (left in each pair) and segmentation overlays (right). Arteries are shown in red, bronchi in green, and non-annotated nuclei in blue.

(F) Registration of BABB-cleared organs to the CUBIC Organ Atlas. For the heart, lung, and kidney, images are shown in the following order: CUBIC Organ Atlas image, BABB-treated sample, sample after atlas mapping, and merged image (green: atlas; red: registered sample).

(G) Validation of segmentation quality in the CUBIC Body Atlas. For each anatomical region, raw image data (left) and the corresponding annotated point cloud (right) are shown. Examples include bone (yellow; regions 1–3); skin (pink) and brain (magenta) (region 4); liver (orange) and intestine (cyan) (region 5); and thymus (yellow), lung (cyan), and heart (red) (region 6).

(H) Validation of whole-body registration accuracy. Red indicates the CUBIC Body Atlas image, and green indicates the registered sample image; yellow denotes areas of good alignment.

(I) Enlarged views of selected slices highlighting alignment quality. Organ-level boundaries show good correspondence, although fine structural details do not always match perfectly.

(J) Registration of a spatial transcriptomics histological image to the CUBIC Organ Atlas. Shown are the original 2D histological image from a published kidney ST dataset, its grayscale conversion, and the registered image onto a corresponding atlas slice. The bottom row shows the 3D cell density atlas image, the matched 2D atlas section, and the final merged image (red: atlas, green: registered ST image).

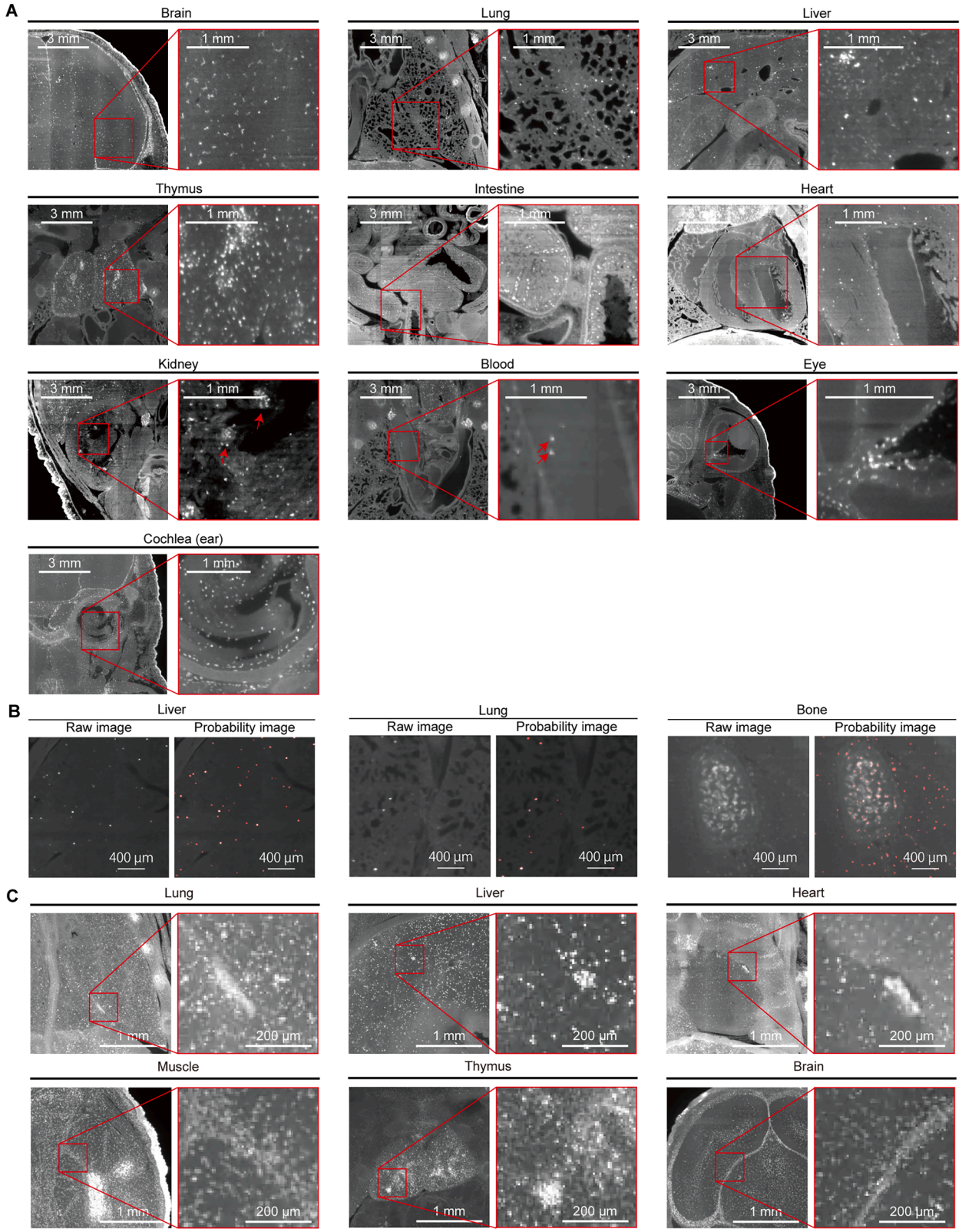

(legend on next page)

Figure S7. Magnified views and probability images from whole-body IBA1 immunostaining, related to Figure 7

(A) Magnified views of IBA1 immunostaining across multiple organs. Representative high-magnification images showing IBA1-positive cells throughout the body. Staining quality was sufficient for reliable detection across diverse tissues.

(B) Raw and probability images of IBA1-positive cells in the liver (left), lung (middle), and bone (right). The left panel shows raw IBA1 immunostaining, and the right panel shows the corresponding probability map indicating detected IBA1-positive cells.

(C) Magnified views of IBA1-positive cell clusters across organs from whole-body 3D immunostaining. Maximum-intensity projections (1,500 μm) highlight the distribution and clustering patterns of IBA1-positive cells in representative organs.